2014

Quantifying submarine eruptive flux from interpretation of hydroacoustic signals, West Mata Volcano, Lau Basin

Chelsea J. (Chelsea Joy) Mack
Western Washington University

QUANTIFYING SUBMARINE ERUPTIVE FLUX FROM INTERPRETATION OF HYDROACOUSTIC SIGNALS, WEST MATA VOLCANO, LAU BASIN

BY
CHELSEA JOY MACK

Accepted in Partial Completion
Of the Requirements for the Degree

Master of Science
Geology

Dr. Kathleen L. Kitto, Dean of Graduate School

Advisory Committee

Chair, Dr. Jacqueline Caplan-Auerbach

Dr. Susan DeBari

Dr. Robert Dziak

MASTER'S THESIS

In presenting this thesis in partial fulfillment of the requirements for a master's degree at Western Washington University, I grant to Western Washington University the non-exclusive royalty-free right to archive, reproduce, distribute, and display the thesis in any and all forms, including electronic format, via any digital library mechanisms maintained by WWU.

I represent and warrant this is my original work, and does not infringe or violate any rights of others. I warrant that I have obtained written permissions from the owner of any third party copyrighted material included in these files.

I acknowledge that I retain the ownership rights to the copyright of this work, including but not limited to the right to use all or part of this work in future works, such as articles or books.

Library users are granted permission for individual, research and non-commerical reproduction of this work for educational purposes only. Any further digital posting of this document requires specific permission from the author.

Any copying or publication of this thesis for commercial purposes, or for financial gain, is not allowed without my written permission.

Chelsea Mack
October 23, 2014

QUANTIFYING SUBMARINE ERUPTIVE FLUX FROM INTERPRETATION OF HYDROACOUSTIC SIGNALS, WEST MATA VOLCANO, LAU BASIN

A Thesis
Presented to the Faculty of
Western Washington University

In Partial Fulfillment of
The Requirements for the Degree
Master of Science

By
Chelsea Joy Mack
October 2014

Abstract

West Mata is a submarine volcano in the northeast Lau Basin. Hydroacoustic data from a 5-month period provide insight into the nature of eruptive behavior at this volcano. Previous studies have used acoustic data to estimate the eruption velocity at subaerial volcanoes (Woulff and McGetchin, 1976; Vergniolle et al., 2004; Vergniolle and Caplan-Auerbach, 2004, 2006; Caplan-Auerbach et al., 2010). In this study, the hydroacoustic data from West Mata are used to calculate eruption velocities and volumes (both lava and gas) for explosions during the 5-month hydrophone deployment. The method used in this study, developed by Vergniolle and Caplan-Auerbach (2006), was found to be most successful when events were hand-picked for a portion of the data during processing, and then extrapolated for explosions from the entire data set. However, there are two factors that contribute to an underestimation of the total eruptive volume. Only one signal type (explosions, representing discrete gas bubble bursts at the volcanic vent) could be used for estimating the eruptive velocities and volumes at West Mata, due to interference resulting from signal reflections. Another issue for accurately estimating cumulative eruptive volume resulted from raypaths reflecting on the sea surface, and arriving at the hydrophones 20 – 80 ms after the direct wave. This also caused hydroacoustic signals to overlap, limiting the calculations to the first 20 ms instead of the entire waveform.

Eruptive velocities for vent explosions recorded at West Mata's four hydrophones were found to range from 2.4 – 24.8 m/s. Eruptive flux ranged from 1.9 – 9.7 m^3/s for each event. The volumes erupted per explosion ranged from 0.03 – 0.15 m^3. Yearly eruption rates were calculated to be $5.7 \times 10^3 – 9.1 \times 10^4$ m^3/yr for both gas and lava. However, if only lava is used (assumed to contain 25% vesicularity), then the yearly eruptive rate at West Mata is

estimated to be $1.9 \times 10^3 – 5.6 \times 10^4$ m^3/yr.

These results were compared to estimates determined from video imagery at West Mata and long-term bathymetric surveys at West Mata and another submarine volcano, NW Rota-1. Velocities estimated from video imagery compare well with velocities estimated from hydroacoustic signals in this study, ranging from 0.2 – 5.2 m/s, compared to a range of 1.0 – 31 m/s using hydroacoustic signals. Volumes estimated from hydroacoustic date are up to three orders of magnitude lower than those derived from bathymetric surveys at West Mata. Given that the results from this study are expected to be an underestimate of eruptive volume, these estimates are considered to be reasonable, suggesting that the hydroacoustic method of estimating eruptive flux is also viable for the submarine environment. It is recommended that future studies deploy hydrophone stations in the near-field (< 5 km) to reduce the effects of sea surface reflections, which would ensure the most accurate results.

Acknowledgements

I would like to acknowledge and thank the following important people:

My thesis committee:

- **Dr. Jackie Caplan-Auerbach** (WWU) for her patience, expertise, and comments and revisions on my thesis
- **Dr. Susan DeBari** (WWU) for her comments and revisions on my thesis
- **Dr. Robert Dziak** (NOAA, Pacific Marine Environmental Laboratory; Oregon State University) for letting me use his data to complete my Masters thesis, and for answering my numerous questions about the data

Delwayne Bohnenstiehl, Andy Lau, Haru Matsumoto, and Matt Fowler, participants in the NSF-funded cruises to West Mata, which gathered the data used in my thesis.

Joseph Resing (NOAA/EOI) and **Kenneth Rubin** (SOEST, University of Hawaii) for their correspondence regarding the video footage used in this study.

Dan Van Pelt (WWU, engineering technology specialist), whose periodic maintenance and work on our lab computers enabled me to process data.

Family, fellow graduate students, and non-geology friends, for your love and support while I completed my Masters degree.

This project was funded by The **Western Washington University Geology Department** and the **Western Washington University Graduate School**.

Table of Contents

List of Figures

List of Tables

I. Introduction

During a 2008 research expedition to the Lau Basin conducted by personnel from the National Oceanic and Atmospheric Administration (NOAA)/Pacific Marine Environmental Laboratory (PMEL), unusually high amounts of particulate matter in the water column were discovered that implied a submarine volcano in the northeast Lau Basin was erupting. A rapid response cruise in May 2009 that gathered direct video observation with the ROV Jason, and near-field hydroacoustic data confirmed that West Mata volcano was indeed steadily erupting. Scientists returned in December 2009 to install a network of four hydrophones surrounding West Mata. These instruments collected hydroacoustic data for a 5-month period during the eruption.

Approximately 75-80% of volcanoes worldwide are submarine (White et al., 2003a), yet the majority of research on actively erupting volcanoes has focused on subaerial volcanoes. Few studies have focused on hydroacoustics of submarine eruptions, and these few have only been in the shallow environment (< 500 m below sea level) (e.g., Chadwick et al., 2008a; Green et al., 2013). Visual observations and instrumentation are easier in the subaerial environment, and to date, the only other observed deep-marine volcanic eruption is from NW Rota-1 in the Mariana Arc (Embley et al., 2006; Chadwick et al., 2008b; Walker et al., 2008; Deardorff et al., 2011). The acoustic data from the 5-month eruptive period at West Mata provide a rare opportunity to conduct a first-hand study in the near-field of the processes associated with early stages of growth at explosive submarine volcanoes over an extended period of time. Other studies of submarine volcanoes (e.g. Axial – Embley et al., 1999; Lo'ihi – Moore et al., 1982; Caplan-Auerbach and Duennebier, 2001; Monowai – Chadwick et al., 2008a) have based their interpretations of eruptive behavior only on eruptive

deposits and seismic behavior, and have used data from long-range instruments. In addition to hydroacoustic data, this study of West Mata provides information from direct video observations, which help to groundtruth the processes occurring in the deep marine environment, and provide important insight into the eruptive behavior (e.g., explosivity, gas content, role of hydrostatic pressure during eruption). Because there is so little information on submarine eruptive activity, these results lay groundwork for better understanding the nature of submarine volcanoes.

The main goal of this study is to use acoustic pressure to calculate eruption velocity and cumulative eruptive volume from gas bubble bursts at West Mata volcano during a 5-month eruptive period. After identifying events with an auto-detection algorithm, events were hand-picked from a subset of the selected data, and their acoustic power was used to calculate velocity and flux, as well as cumulative eruptive volume at West Mata. Values for eruptive velocity and cumulative volume were found to be consistent with estimates from short videos filmed during the eruption and from long-term changes determined with bathymetric surveys at West Mata. Results from this study lay groundwork for future studies of deep-marine explosive volcanism where scientists could use hydroacoustic data to estimate eruption velocity, flux, and volume at any erupting submarine volcano.

Other topics investigated in this study include the effects of signal multipathing and signal reflections on the data, whether event detection can be automated, or if it is necessary to identify events by hand, and if the amplitude of explosions obeys a power law distribution.

II. Background

Geologic setting

West Mata volcano is located in the northeast Lau Basin, in an area of significant local tectonic complexity (figure 1). The Lau Basin, bounded by the Lau Ridge to the west and the Tonga Ridge to the east, is contained within the northeast corner of the Indo-Australian Plate, and a number of backarc spreading centers in the Lau Basin define the Niuafo'ou and Tonga Microplates (Zellmer and Taylor, 2001). West Mata lies at the north end of the Tonga Arc, with its summit approximately 1200 meters below sea level (Resing et al., 2011). To the north and east of the volcano (60 – 140 km, respectively) is the boundary between the Indo-Australian Plate and the Pacific Plate. As the Indo-Australian Plate terminates 60 km north of West Mata, it transitions from a subducting boundary to a left-lateral strike-slip plate boundary approximately 100 km to the northwest of the volcano (figure 1). Seismic evidence and bathymetric data in the northeast corner of the Indo-Australian Plate indicate that the Pacific Plate is tearing at the north end of the Tonga Trench as it moves westward relative to the Australian Plate (Millen and Hamburger, 1998), which may possibly be responsible for a series of NE-SW tears in the northern Tonga Microplate (Resing et al., 2009). Thus, the tectonic frame around West Mata volcano includes all three major types of plate boundaries.

The Discovery of West Mata's Eruption

Direct observations of eruptive activity at deep submarine volcanoes are difficult because of the challenges associated with deep-sea exploration and observation (i.e., remoteness, lack of visibility), making it difficult to identify when and where submarine volcanic eruptions are occurring. However, a research expedition in 2008 led scientists from

NOAA/PMEL to conclude that a deep-sea volcanic eruption was occurring in the northeast Lau Basin. The initial goals of the 2008 Lau Basin expedition were to conduct water-column plume surveys in the region and conduct bathymetric mapping. The target areas for this expedition were the Mangatolu Triple Junction, the Northeast Lau Spreading Center (NELSC), and Niuatahi (known at the time as Volcano "O"), a large caldera on the seafloor (figure 2; Merle, 2008). However, during the time that the R/V Thompson was sailing over West Mata, attention was directed to unusually high concentrations of hydrogen and methane in the water column, indicating magma-seawater interactions taking place on the seafloor (Baumberger et al., 2009; Merle et al., 2009; Resing et al., 2011). Eager to take advantage of the opportunity to study this deep-sea eruption, scientists returned to West Mata on a rapid response cruise in May 2009. During dives by the ROV Jason the volcano was observed to be actively erupting from two summit vents. The eruption of West Mata is only the second observation of active deep (> 500 m) submarine volcanic eruptions. The first such eruption observed was at NW Rota-1 in the Mariana Arc, whose summit is 517 m below sea level (Embley et al., 2006; Chadwick et al., 2008a; Walker et al., 2008; Deardoff et al., 2011).

The rapid response cruise during May 2009 recovered a hydrophone deployed in the NELSC on the initial 2008 cruise (deployed from December 2008 to May 2009), and deployed two temporary hydrophones within 20-30 m of Hades vent. These were deployed for less than 24 hours at a time, with the goal of providing simultaneous video footage and hydroacoustic data. Videoes taken from the ROV Jason in May 2009 confirmed that West Mata was indeed steadily erupting (Resing et al., 2009). Video clips (available at oceanexplorer.noaa.gov) show active degassing causing predominantly explosive eruptions, with some accompanying effusive activity. The nearly continuous explosive eruptions

produced abundant volcaniclastic material. Lobate lava flows and pillow basalts were also found near the two active vents of the volcano and on its flanks (Resing et al., 2011).

A long-term network of four hydrophones surrounding West Mata (figure 3) was installed on a separate expedition in December 2009 (Bohnenstiehl et al., 2010; Dziak et al., 2010). These hydrophones continuously recorded hydroacoustic data from December 2009 to April 2010[1] at a sample rate of 1000 Hz. Distances from West Mata's summit to each of the stations ranges from approximately 5 km to approximately 20 km (figure 3), the south station being the closest.

The hydrophones are connected to an anchored mooring, and are suspended in the Sound Fixing and Ranging (SOFAR) channel (the depth of minimum sound velocity; Barbour and Woollard, 1949). The east, west, and north stations are suspended at depths of 897 m, 955 m, and 912 m, respectively, coincident with the depth of the SOFAR channel in this region. However, mislabeling during deployment caused the south station to be suspended at a depth of only 230 m (Dziak, pers. comm, 2013), approximately 800-1000 m above the SOFAR channel (figure 4).

West Mata volcano: morphology, deposits, and lava geochemistry

West Mata volcano is somewhat conical in shape, and rises from depths of 2900 m to 1160 m at the summit. It contains a WSW-ENE striking ridge, formed by pillow lavas and flows, whose orientation along the ridge of the entire volcano suggest that the ridge is oriented in the direction of most compressive stress, allowing for dikes to intrude and widen perpendicular to the ridge. This ridge orientation reflected in the northeast Lau Basin could

[1] Any reference hereafter to the "5-month study" is referring to data recorded during this time period.

also be influenced by the tearing of the Pacific Plate as it subducts under the Indo-Australian Plate (Resing et al., 2009; Clague et al., 2011). Ridge morphology includes some lava plateaus, but overall shows a gradual downward-sloping pattern. The northeast and southwest flanks of West Mata are relatively smooth compared to the morphology of the ridge, suggesting that they are mantled in volcaniclastic debris formed by explosive volcanic activity. Two vents, named Hades and Prometheus, are located northwest of the summit, at depths of 1205 and 1175 m, respectively. Activity observed during the rapid response cruise shows volcanic activity at both of these vents. Although video imagery only shows activity at one vent at a time, it is plausible that both vents could have been erupting simultaneously (Clague et al., 2011). Because Hades' eruptive style was primarily extrusive with gas bubble explosions, and explosive fire fountaining was observed at Prometheus (Resing et al., 2009), simultaneously erupting vents would generate a mixture of hydroacoustic signal types seen across the four hydrophones during this 5-month study.

Geochemical analysis of fresh lava samples from West Mata indicate that the volcano actively produces boninite, a rare rock and product of subduction-related melting (Resing et al., 2011). Boninites are formed in the mantle wedge as the subducting plate emits large volumes of volatiles, namely H_2O and CO_2. Most boninites observed in the rock record are ancient, as they are thought to erupt when subduction is initiated at a boundary. To date, active boninite formation has only been observed at West Mata. Because the subduction zone at the Pacific-Australian plate boundary is old, it is unusual to see boninites actively forming (Resing et al., 2011). West Mata's high content of CO_2 and H_2O (11 ppm CO_2, 0.90-0.94% H_2O) may also provide an explanation for the amount of gas and degree of explosivity observed in West Mata eruptions (Resing et al., 2011).

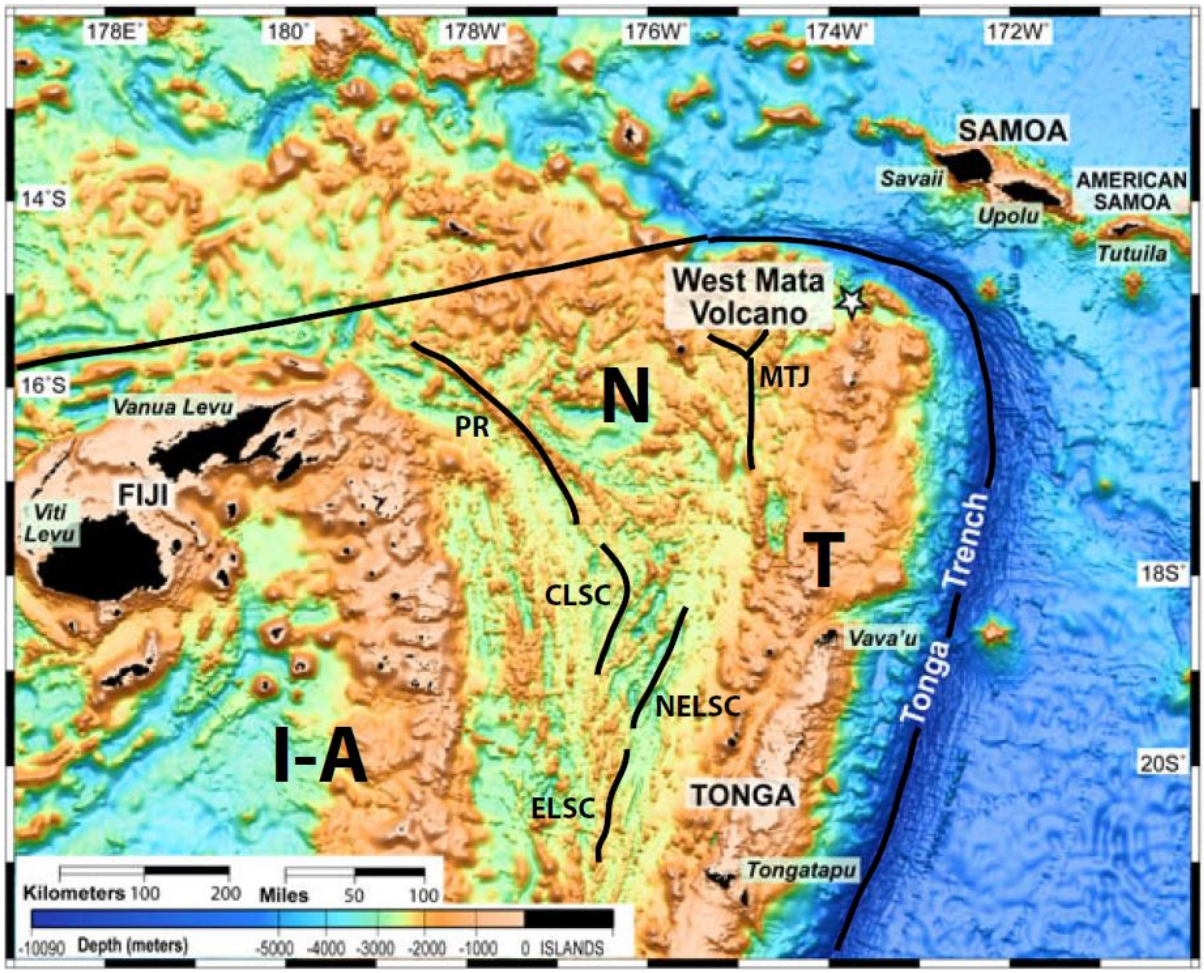

Fig. 1. West Mata's location at the northeast corner of the Lau Basin. West Mata (white star) lies on the Tonga Microplate (T), in the corner of the Indo-Australian (I-A) Plate, and is surrounded by three different plate boundaries: a subduction zone to the east, a strike-slip boundary to the north, and a spreading center to the southwest. This places West Mata in one of the most locally complex tectonic settings on the planet. Figure modified from PMEL (Earth-Ocean Interactions Group, NOAA). Other features: Niuafo'ou Microplate (N), Peggy Ridge (PR), Central Lau Spreading Center (CLSC), Northeast Lau Spreading Center (NELSC), Eastern Lau Spreading Center (ELSC).

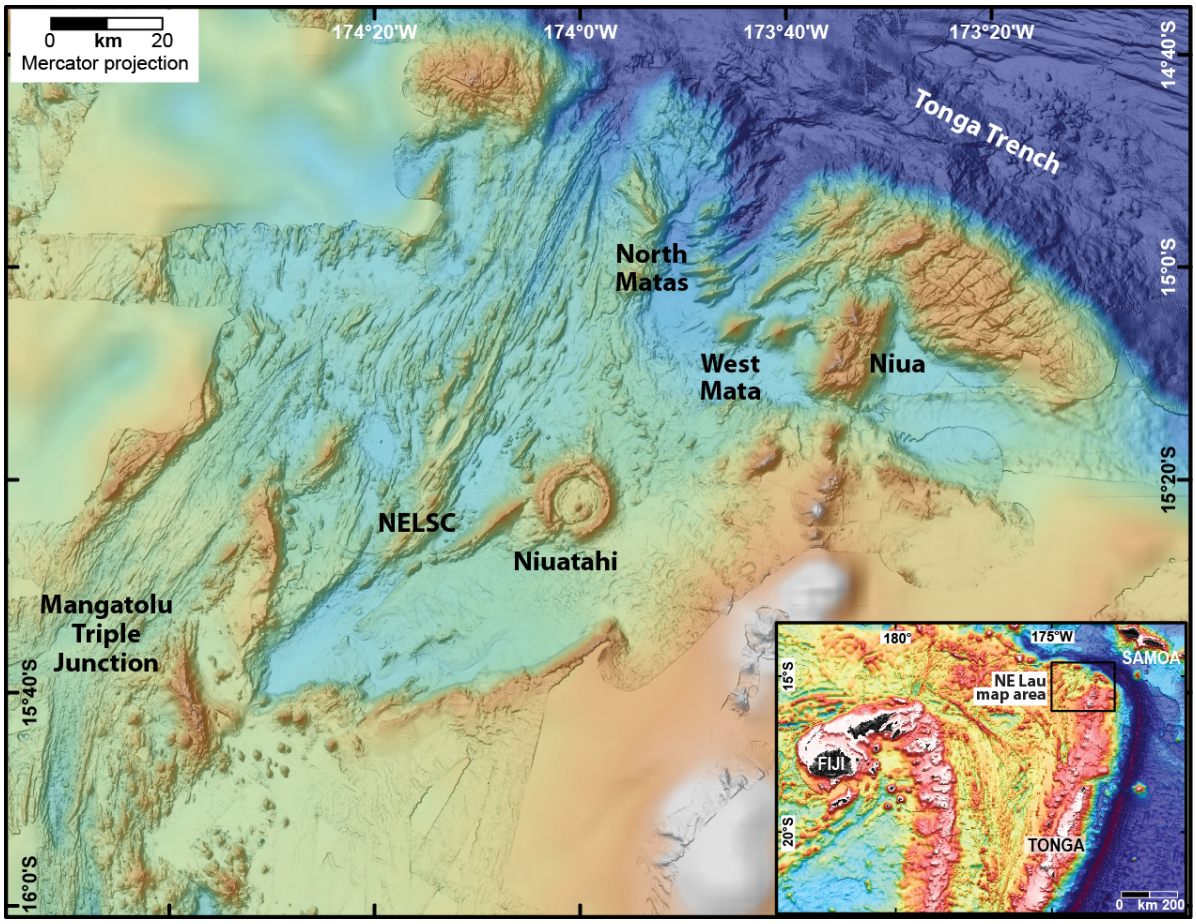

Fig. 2. Map of the northeast section of the Lau Basin (see inset on the lower right corner). The original research expedition in 2008 targeted areas in the northeast Lau Basin, including the Mangatolu Triple Junction, the Northeast Lau Spreading Center (NELSC), and Niuatahi (Volcano "O"). Also note that the linear features around West Mata, the North Matas, and north of Niua strike NE-SW, and may be a result of rifting at the northeast corner of the Pacific Plate, or compressive stresses (Resing et al., 2009; Clague et al., 2011). Figure courtesy of Merle (2012).

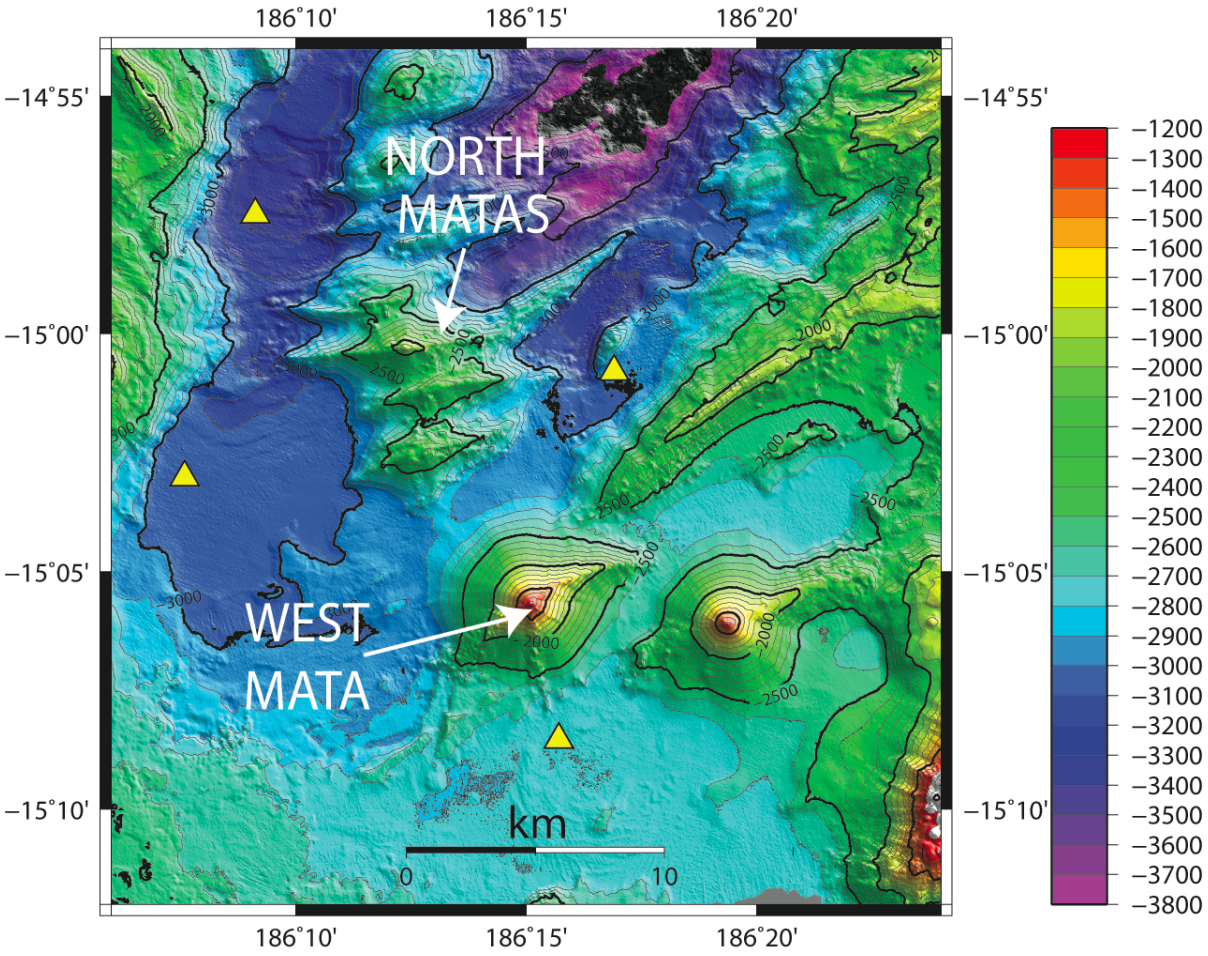

Fig. 3. A network of 4 hydrophones (yellow triangles) was deployed around West Mata during a cruise led by PMEL in December 2009. These hydrophones recorded continuously at a rate of 1000 Hz from December 2009 to April 2010, for a 5-month period (143 days).

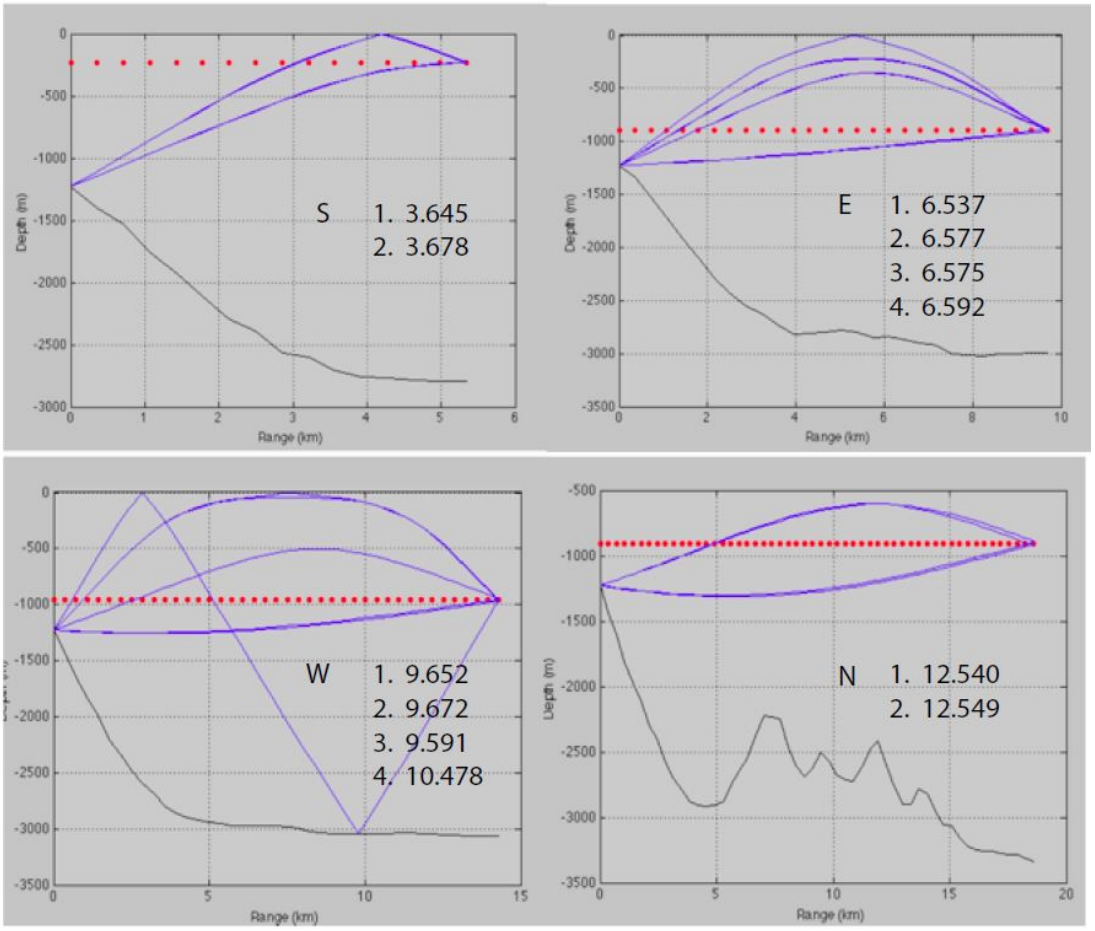

Fig. 4. Acoustic raypaths based on models of sound velocity in the West Mata region (figure courtesy Del Bohnenstiehl). Dotted red lines show depth of hydrophones. Plots are arranged in order of increasing distance from WM summit: south (upper left), east (upper right), west (lower left), and north (lower right). Numbers listed for each station are travel times in seconds for each raypath. Note that the north station is the only one that does not have a seasurface reflection of the soundwaves. However, signals from the direct and refracted raypaths arrive at almost the same time, causing signals at the north station to add constructively, amplifying the recorded signal. The east and west stations also have several waves arriving in a short time frame (20-80 ms), also causing the signals to add constructively and out of phase, amplifying the recorded signal for direct waves; reflected sound waves alter the shape and amplitude of the signal.

III. The Physics of Volcano Acoustics

How sound propagates

In an elastic medium (such as air or water), sound is communicated between neighboring molecules as it is produced at a source and radiates outward. Motion of these molecules is parallel to the direction of sound propagation, and is oscillatory due to the nature of the elastic medium. As this oscillatory motion of the molecules is set in motion, it creates areas of a greater density of molecules (compression) and areas with a lesser density of molecules (rarefaction). The sound wave spreads out from the source in all directions as the molecules oscillate (Urick, 1975; Speaks, 1992). Figure 5 illustrates this concept using a tuning fork.

Activity at volcanic vents produces sound, and the basic physical responses of the medium surrounding the volcanic vent are the same as described above, whether the sound waves are traveling through air or water. Driven by overpressure of the gas rising within the conduit, volcanic material will exit the vent, producing sound as gas bubbles at the vent oscillate before bursting (Vergniolle and Brandeis, 1994, 1996; Vergniolle et al., 1996; Vergniolle et al., 2004). This oscillation of the gas bubble induces a pressure wave, which sets the air (or water) molecules into motion in a pattern that spreads outward from the volcanic vent. These sound waves produced at the vent are recorded on microphones placed on the flanks of the volcano in subaerial environments, and on hydrophones suspended in the water column or deployed on the seafloor in submarine environments. When the sound reaches the microphone, a pressure-sensitive piezolectric crystal inside registers changes in pressure. Areas of compressed air/water molecules will be recorded as a positive pressure,

and areas of rarefaction are recorded as negative pressure. An example of compression and rarefaction at West Mata interpreted to be a gas bubble bursting at one of the volcano's summit vents is shown in figure 6.

Specific types of volcanic activity and the corresponding sounds they produce are described in further detail below under "Previous Work."

The SOFAR Channel

The SOFAR channel defines the depth in the ocean at which the speed of sound is at its minimum; the axis of the channel is where sound travels slowest (figure 7). Sound speed in water is affected by temperature and pressure, and to a lesser degree, salinity. At mid-latitudes, the sound speed minimum is located at approximately 1000-1200 m depth (DOSITS website; Urick, 1975), which is close to West Mata's 1160 m summit and eruptive vents (1205 m and 1175 m depth). Because waves will refract and bend toward areas of lower velocity, sound waves traveling within the SOFAR channel will continuously refract toward the axis as they travel, causing them to be trapped in this depth range over larger lateral distances (Barbour and Woollard, 1949). The effects of the SOFAR channel on sound waves emitted from West Mata's summit are investigated in further detail below.

Volcano Acoustics

There are three different types of sources that generate sound: monopole, dipole, and quadrupole (Lighthill, 2001 – see figure 8). A monopolar source (figure 8a) is one that causes sound to radiate equally in all directions, spreading spherically (Woulff and McGetchin, 1976; Vergniolle and Brandeis, 1994; Johnson and Lees, 2000; Matoza et al.,

2010). One example of a monopolar source of sound is an explosion. A dipolar source (figure 8b) is one in which two monopolar sources of equal strength operate simultaneously, but in opposite phase, so that while one monopole is creating areas of compression, the other is creating areas of rarefaction. Dipoles have a tendency to focus sound in a specific direction, and therefore any source that focuses sound (e.g., a conduit wall) is considered as a dipolar sound source. A quadrupolar source (figure 8c) is one in which two dipoles of equal strength operate simultaneously, but also in opposite phases. Quadrupolar sources of sound are typically seen in situations where noise is generated by turbulent jetting of gases. The signals used in this study – which represent bursting gas bubbles – generate sound from a monopolar source (other types of volcanic activity may be generated by a different source type; see Woulff and McGetchin, 1976 for examples). Also, monopolar sources of sound experience irregular flux of material; gas bubbles burst intermittently, providing an irregular flux of gas and lava through time (Woulff and McGetchin, 1976). Calculations similar to those in this study also assume a monopole source for a circular flat orifice, represented by the volcanic vent (Vergniolle et al., 2004; Vergniolle and Caplan-Auerbach, 2004).

Regardless of the type of source generating sound (monopole, dipole, or quadrupole), there are two main ways that sound will spread in the ocean. The first is a case in which the sound is generated at a point source, and will spread evenly and homogenously in all directions. The intensity of the sound in this case will be evenly distributed across a spherical surface surrounding the source, and will decay as a function of $1/r^2$, where r is the distance from the source to the receiver. In the other scenario – such as when sound travels through the SOFAR channel – the soundwave will be bounded by upper and lower planar boundaries, and the intensity of the sound will be evenly distributed across a cylindrical

surface as it radiates outward from the source. With cylindrical spreading, the intensity of the sound wave decays as a function of 1/r as it travels from source to receiver (Jensen et al., 1993). Figure 4 shows that the paths of sound to the south station propagate in a nearly linear path, indicative of spherical spreading in which there is no refraction. However, it is evident from figure 4 that the raypaths to east, west, and north stations curve into the SOFAR channel as they travel, suggesting that the sound will be bounded by refraction within the sound speed minimum, and sound will spread cylindrically to these three farther stations. This is in accordance with the fact that cylindrical spreading of sound applies only for longer ranges in the ocean (Jensen et al., 1993).

In the subaerial environment, there are atmospheric factors that can slightly alter the spreading sound wave, affecting the sound wavefront and the resulting amplitude of the signal recorded on the microphone. Johnson (2003) noted that variations in air temperature and wind speed could create areas of either amplified sound, or shadow zones in which no sound waves propagated. In the submarine environment, these factors would likely translate to ocean currents and ocean temperature variation. However, ocean temperatures are only expected to vary up to 1-2 °C, and ocean currents do not typically vary enough at the depths of the hydrophones in this study, nor do they change significantly on a short (less than a year) time scale to be considered a significant external factor. Ocean temperature and current variations are therefore not considered in this study (Jensen et al., 1993). However, Johnson (2003) did also note that other factors of sound attenuation – namely reflection – can cause amplitude decay of the signal. This, as well as refraction of sound, are two complications that were considered when processing the signals from West Mata.

Previous Work

Studies at subaerial volcanoes have shown that different types of eruptive activity produce distinct seismic and acoustic signals (Vergniolle and Brandeis, 1994, 1996; Johnson and Lees, 2000; Matoza et al., 2007; Petersen et al., 2006). These behaviors include acoustic tremor (Johnson and Lees, 2000; Lees et al., 2008; Matoza et al., 2010; Fee et al., 2010; *McNutt, 2005,* Ripepe et al., 1996), chugging (Johnson and Lees, 2000; Lees et al., 2004; Lees et al., 2008), sustained/continuous degassing (Fee et al., 2010; Johnson and Lees, 2000; Matoza et al., 2010), discrete gas bubble bursts (Johnson and Lees 2000; Johnson, 2003; Vergniolle and Brandeis, 1994, 1996), and ash-rich plumes (Petersen et al., 2006; Caplan-Auerbach et al., 2010). Seismic and acoustic data can therefore be used as a window into the eruptive behavior of volcanoes that cannot be observed. Because there are no seismic data from West Mata, this study will only focus on acoustic signals.

Acoustic tremor is a continuous signal that contains narrow bands of infrasonic (i.e., <20 Hz) frequencies, typically with dominant frequencies in the range of 0.5 – 3 Hz (Lees et al., 2008; Fee et al., 2010; Matoza et al., 2010). Frequencies as high as 8 Hz can be seen at some volcanoes (Ripepe et al., 1996; Lees et al., 2004). Tremor signals can contain asymmetric amplitudes (Lees et al., 2004; Lees et al., 2008). Acoustic tremor generally is strongest at one fundamental frequency (non-harmonic, or monochromatic, tremor – Ripepe et al., 1996; Matoza et al., 2010), but in some cases, harmonic integer overtones can be produced, yielding more than one strong band of frequency (harmonic, or polychromatic, tremor – Lees et al., 2004; Fee et al., 2010). In both cases, acoustic tremor can exhibit a phenomenon known as "gliding," in which the bands of strongest frequencies vary slightly over time, rather than remaining at one frequency. In some cases, such as Karymsky volcano

(Johnson and Lees, 2000; Lees et al., 2004; Lees et al., 2008), acoustic tremor can contain regular pulses throughout time, in which case it is referred to as chugging (figure 9).

Sustained degassing produces diffuse signals, which are another common signal type seen in volcanic acoustic data. Acoustically, these signals can have an impulsive beginning (Johnson, 2000; Johnson 2003) and last for several minutes, with varying intensities (Johnson 2003; Vergniolle and Caplan-Auerbach 2006). For subaerial volcanoes the frequency content is strongest between 0-5 Hz (Vergniolle and Caplan-Auerbach, 2006), although some cases show signals with significant energy in higher frequencies up to 6-12 Hz.

A third common signal type is a short-duration, discrete signal associated with gas bubble bursts. In subaerial settings, these signals contain frequencies up to 8 Hz, and have an impulsive onset with two to three amplitude peaks, and are followed by a coda with much lower amplitude (figure 10; Vergniolle and Brandeis, 1994, 1996a, 1996b; Johnson and Lees, 2000; Rowe et al., 2000; Johnson, 2003; Vergniolle and Caplan-Auerbach, 2004; Vergniolle et al., 2004). These discrete signals can repeat in regular pulses (Vergniolle and Brandeis, 1996a, 1996b; Vergniolle and Caplan-Auerbach, 2004). Similar signals have also been seen at Erebus (Rowe et al., 2000), Shishaldin (Vergniolle et al., 2004; Vergniolle and Caplan-Auerbach, 2004), Tolbachik, Kluychevskoi, Stromboli, Arenal, and Karymsky (Johnson, 2003; figure 11).

Because subaerial networks generally sample at a rate of 100 Hz, the Nyquist frequency limits the maximum recorded frequency to 50 Hz, and therefore signals above 20 Hz are difficult to clearly detect. Data at West Mata are recorded at a sampling rate of 1000 Hz, allowing frequencies up to 500 Hz to be recorded. Thus the recorded spectral content expected at West Mata is not the same as in subaerial systems.

A handful of previous studies on subaerial volcanoes have used acoustic pressure to determine eruption velocity. Woulff and McGetchin (1976) were the first to use acoustic pressure to calculate the velocity of gases in fumaroles on Volcan Acatenango in Guatemala. Later studies by Vergniolle et al. (2004) and Vergniolle and Caplan-Auerbach (2004, 2006) applied this method to estimate the eruption velocity of basaltic ash plumes at Shishaldin volcano in Alaska, and Caplan-Auerbach et al. (2010) applied this method for ash-rich plumes at Augustine volcano, also in Alaska.

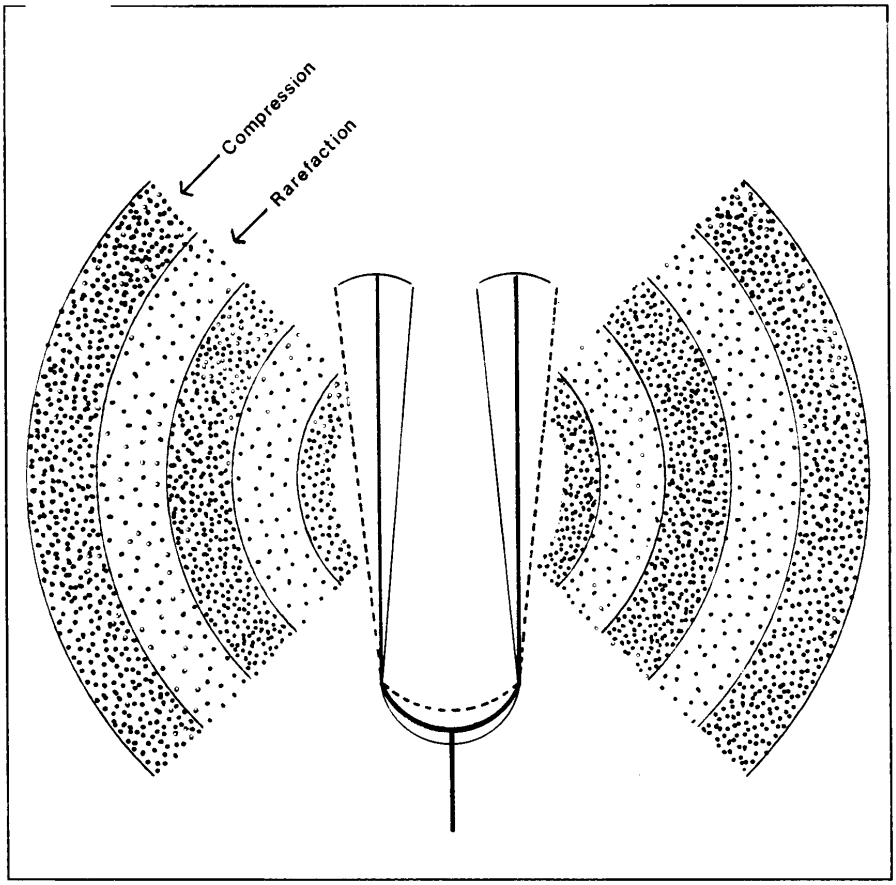

Fig. 5. Figure 1-4 from Speaks (1992) shows a tuning fork creating wavefronts of compressed and rarefied air molecules. When the tuning fork is set into motion, it vibrates in such a way that the two tines will repeatedly moving toward and away from each other. This pattern of vibration creates the resulting areas of compression and rarefaction.

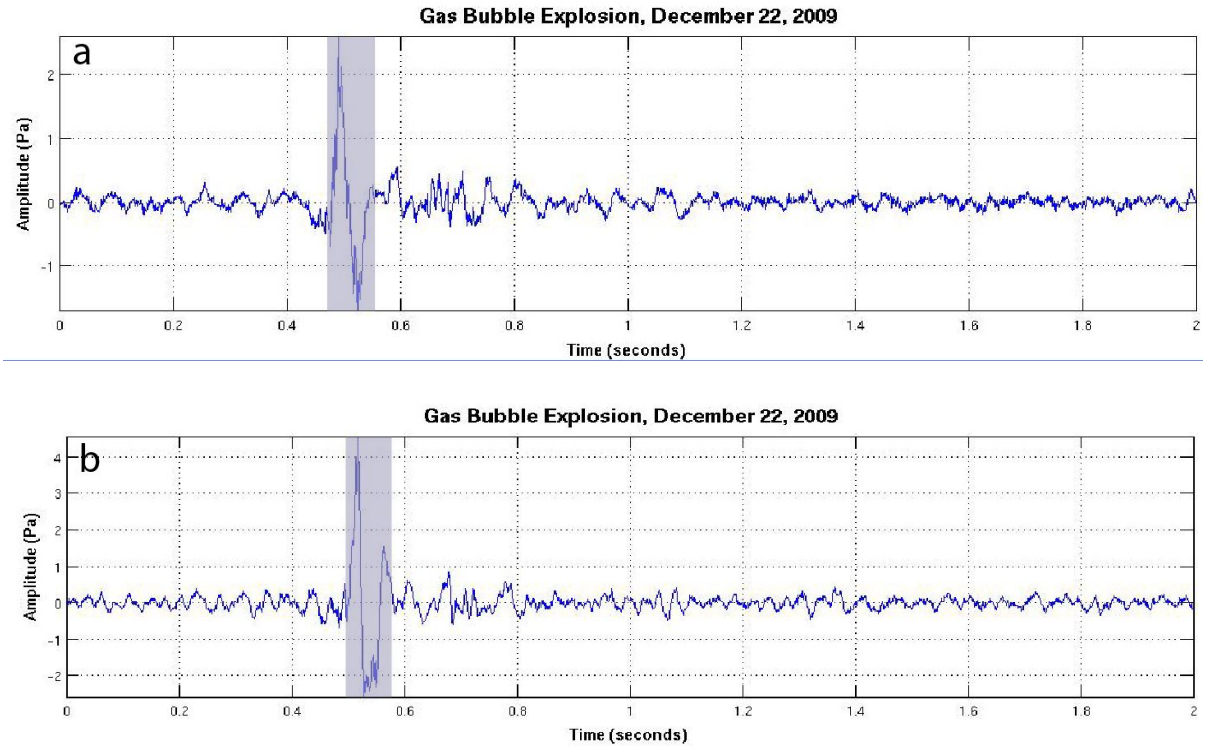

Fig. 6. Two examples of bubble explosions (highlighed in blue), recorded by the south station at West Mata on December 22, 2009. Positive values in the time series above represent compression of water molecules, and negative values represent rarefaction of water molecules as the sound travels outward from West Mata's summit vent. Typically, bubbles will complete approximately one to one and a half cycles of oscillation before bursting. This creates an initial positive peak pressure, followed by a larger negative peak pressure, and typically a second (and smaller) positive peak pressure prior to the coda, at which point the gas bubble has burst. Video footage at West Mata's Hades vent confirms both the growth and contraction of these bubbles.

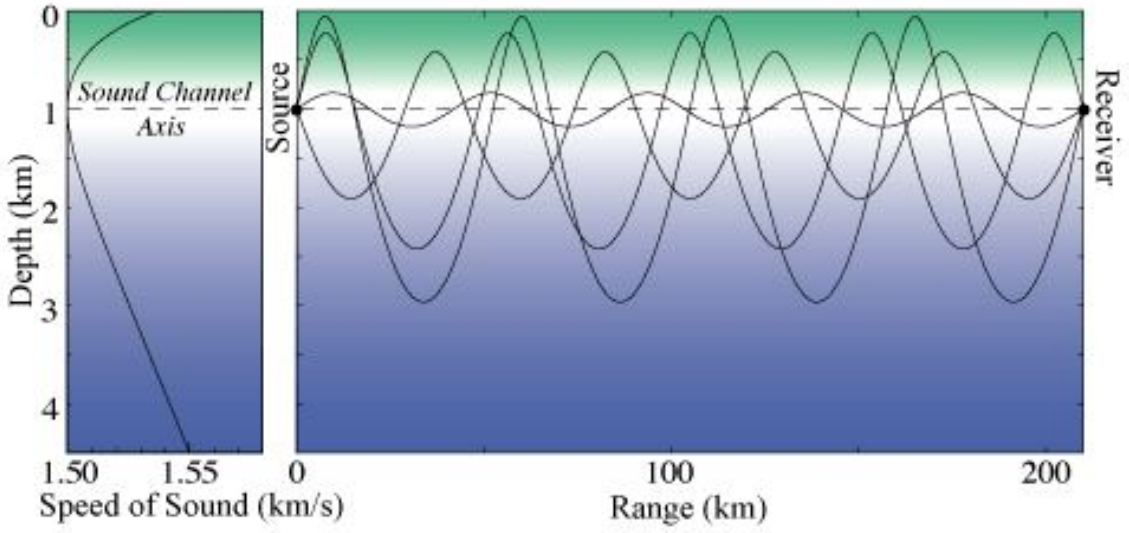

Fig. 7. Illustration of the speed of sound with depth (left) and possible raypaths of sound within the SOFAR channel (right). The speed of sound in the ocean is controlled by pressure, salinity and temperature. As the soundwaves travel from the source to the receiver, they constantly bend toward the sound channel axis (right), where the sound speed is at its minimum. Note that the y-axis (depth) is vertically exaggerated in the above figure. Only waves with an angle from the sound channel axis of 12 degrees or less will remain within the SOFAR channel upon propagation. Figure courtesy of the "Discovery of Sound in the Sea" website (www.dosits.org).

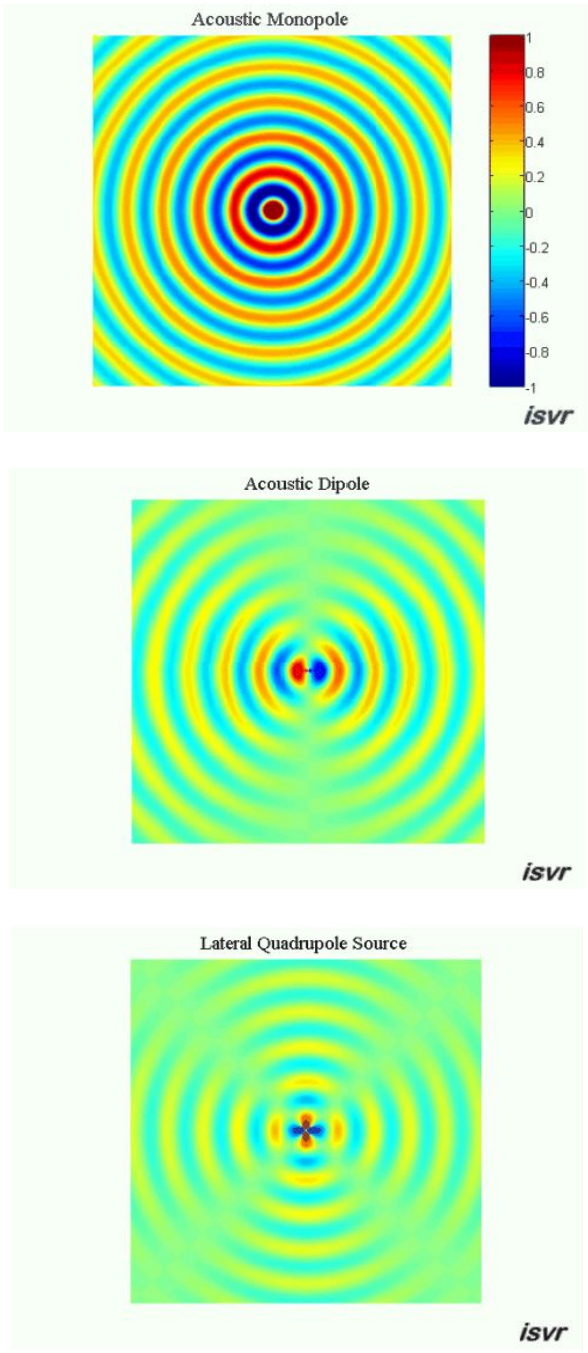

Fig. 8. Examples of monopolar, dipolar, and quadrupolar radiation. Red areas indicate positive amplitude (compression), and blue areas indicate negative amplitude (rarefaction). Figures are from the Institute of Sound and Vibration Research (ISVR) website.

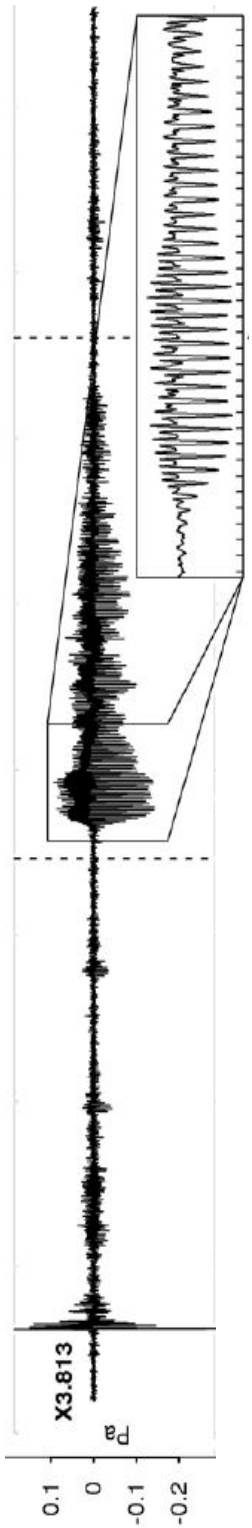

Fig. 9. A type of periodic harmonic tremor known as chugging at Reventador volcano in Ecuador. Chugging typically shows an gradual onset and decay, with asymmetric amplitudes and regular pulses. Figure modified from Lees et al. (2008).

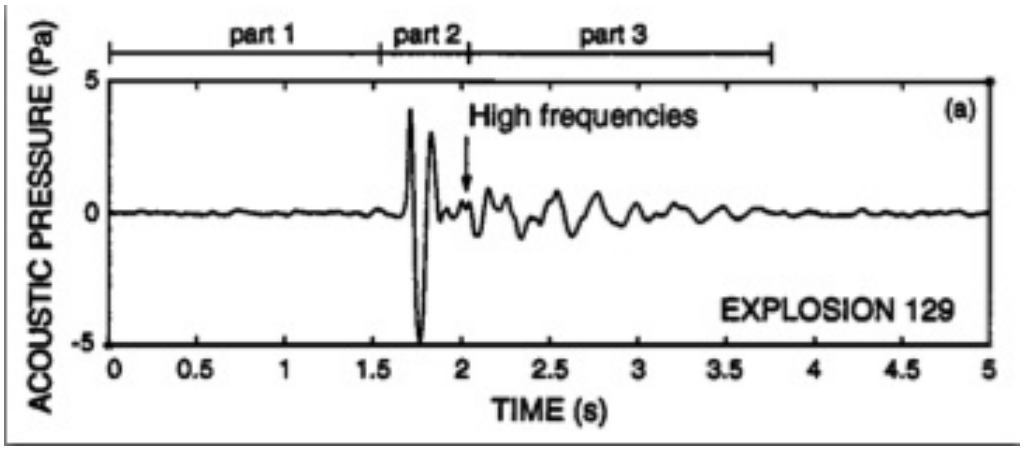

Fig. 10. . Waveform for a gas bubble explosion at Stromboli (Vergniolle and Brandeis, 1994). The signal contains two to three amplitude peaks, followed by a lower amplitude coda. Similar signals have also been seen at West Mata (see figure 6).

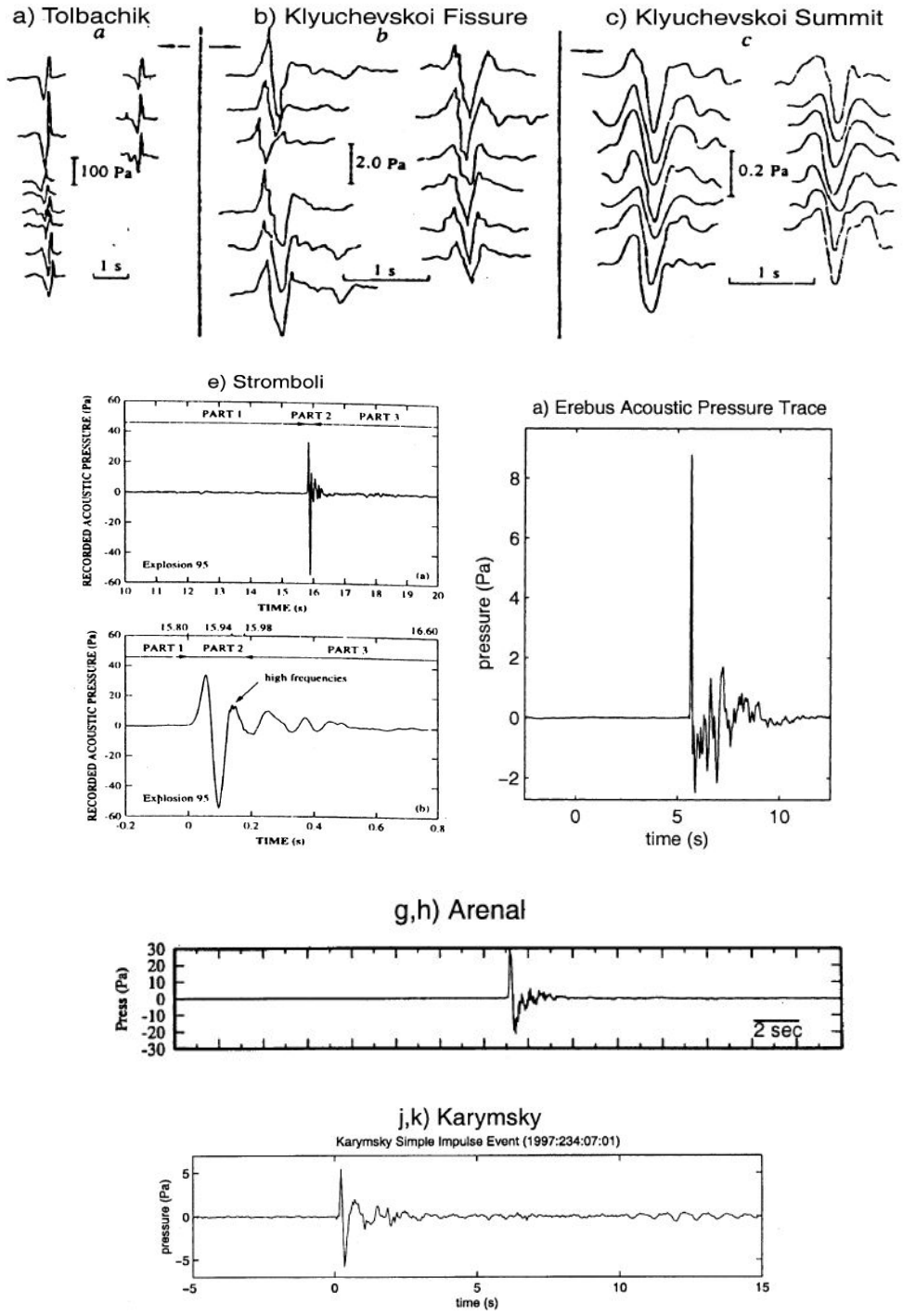

Fig. 11. Examples of gas bubble explosions from various volcanoes around the world. Note that even among different volcanoes, gas bubble explosions all contain two to three peak amplitudes, followed by a smaller amplitude coda. Figures are from Johnson, 2003 (figures 1, 3).

IV. Methods

Overview

The goal of this study was to use acoustic pressure to calculate eruptive velocities and cumulative eruptive volume at West Mata during the 5-month hydrophone deployment from 2009-2010. Because this has been successfully accomplished for volcanoes in the subaerial environment (Woulff and McGetchin, 1976; Vergniolle et al., 2004; Vergniolle and Caplan-Auerbach, 2004, 2006; Caplan-Auerbach et al., 2010), this study aims to determine whether this method is also valid for the submarine environment. To accomplish this goal, the first step was to catalog the different signal types seen during the 5 months of data collection, and choose which event types could be used for analysis. Once events were detected, eruption velocity and event eruptive volume were calculated using the algorithm presented by Vergniolle et al. (2004). Finally, cumulative eruptive volume was calculated for the 5-month eruption. These results were compared with three alternate methods of calculating eruption velocity and cumulative volume (both instantaneous and long-term) at West Mata.

Cataloging signal types

Reviewing and characterizing the types of signals seen at West Mata was performed using Antelope, a database program that graphically allows the user to look at large amounts of data. For the 5 months of hydroacoustic data recorded at West Mata, two main signals were seen: diffuse and discrete, with other time periods dominated by non-volcanic signals (e.g. T-phases) or volcanic tremor.

Diffuse signals (which are interpreted to be continuous degassing) at West Mata last

from several seconds to several minutes, and contain broadband frequencies up to 400 Hz (figure 12a) that are approximately equal in strength. Diffuse signals can also contain strong spectral bands below 100 Hz (figure 12b). The waveforms of diffuse signals vary in amplitude, and have an emergent beginning and gradual decay, although some periods of time show very impulsive starts and abrupt endings (figure 12b). The diffuse signals that show rapid onset and termination are thought to be caused by a magma quench cap that causes pressure to build in the conduit, until the cap opens like a trap door at the sudden release of gas, and closes once the pressure has been released (Dziak et al., 2013). Video footage from the rapid response cruise to West Mata in early 2009 confirms that there is a quench cap of lava at Hades vent that acts as a lid that allows gases to escape (Quench_Cap; Appendix I). This causes a cyclic process of pressure build up and rapid degassing at West Mata.

West Mata's discrete signals (figure 13a) can either occur alone, such as in figure 6, or they may be superimposed on diffuse signals (figure 13b). Like the discrete signals seen at several subaerial volcanoes (see figures 10, 11), West Mata's discrete signals generally contain one positive amplitude peak followed by a negative peak (one cycle) that lasts between 20 and 100 ms before the coda begins (e.g., see figure 6). Some of these signals are seen to contain 3 peaks (one and a half cycles – figure 6b) before the coda, instead of 2 (figure 6a), although these occur less frequently. Broadband frequencies up to 400 Hz are seen, with strongest signals below 10 Hz.

These discrete signals are interpreted to be single gas bubble explosions at one of West Mata's eruptive vents (e.g. Rowe et al., 2000; Vergniolle and Brandeis, 1994, 1996), and are observed to occur as frequently as 5 - 27 events per minute. Although video imagery

of West Mata's eruptive activity is sparse, the frequency and nature of gas bubble bursts in a 2009 video from Joseph Resing (PMEL/NOAA) suggests that this range of 5 – 27 events per minute is reasonable. Because there are two vents at West Mata that produce different eruptive activities (Merle, 2009), it is plausible that they could have been erupting simultaneously during the 5-month hydrophone deployment. This could provide an interpretation for the mix of discrete and diffuse signals seen periodically (figure 13b). While the video imagery was only able to show eruptive activity at one vent at a time; the hydroacoustic data show sounds emitted from the entire volcanic system, which could include simultaneous (and different) eruptive activities at Hades and Prometheus.

Tremor at West Mata is much harder to identify, because it is generally not a dominant signal type at West Mata, and also because of its similarity in waveform to diffuse signals. Spectrograms are the best method for identifying tremor, as it identifies the fundamental strong frequency, which is a signature characteristic of tremor (figure 15a; cm_mata_spec.m; Appendix II) – typically between 0 and 5 Hz – that is also commonly seen in tremor at subaerial volcanoes, (Hagerty et al., 2000; Fee et al., 2010). Waveform amplitudes of West Mata's tremor contain regular pulses, and can sometimes be slightly asymmetric (figure 15b). Because tremor is not a dominant signal type during the 5-month study, it is not included in the signal cataloging.

An additional frequent but non-volcanic signal seen at West Mata was T-phases. When submarine earthquakes occur and seismic waves couple into the water column, they travel as sound waves through the water and are known as tertiary waves, or T-phases. Waveforms for T-phases bear similarity to those seen in seismic data that represent earthquakes (Dziak et al., 2009). T-phases were the dominant signal type during only a very

small part (5%) of the 5-month hydrophone deployment (figure 14). Most signals from T-phases arrive first at the northern station, suggesting that they come from a source other than West Mata

There is an apparent banding of frequencies in the signals at West Mata suggestive of harmonics. This is an interference pattern caused by constructive and destructive interference of waves. At West Mata, the sound waves will travel in two paths, one leading directly from the source (volcanic vent) to the receiver (hydrophone), and the other starting at the source and reflecting off the sea surface before it travels to the receiver. When the sound waves reflect off the sea surface, they undergo a phase change of 180 degrees (positive amplitudes become negative, and vice versa). If the distance traveled by the direct and reflected waves were the same, then the signals would arrive at the hydrophone simultaneously, canceling out entirely. However, the reflected wave travels a slightly longer distance, and arrives in the middle of its direct counterpart. This offset in arrival time of the direct and reflected waves causes certain frequencies to either cancel out or to amplify. This produces an interference pattern at the hydrophone known as the Lloyd's Mirror Effect. At the distance and depth at which the south station is suspended these alternating bands are seen every ~30 Hz, indicating that sound waves experience destructive interference for frequencies in multiples of 30 Hz. Despite their similarity to harmonics observed during many tremor sequences, these patterns are a path effect, not a source effect.

Once the three signal types seen associated with volcanic activity at West Mata – diffuse, discrete, and T-phases – were defined and categorized, the percentage of each signal's occurrence and duration during the 5 month hydrophone deployment was recorded

(figure 16). Total percentage of each signal type during the study was determined by tallying up daily total percentages.

For the 5-month deployment, 62% of the total signals seen were diffuse, 36% were discrete, and the remaining 2% consisted of T-phases. Quiescent times at West Mata – times during which very low amplitude signals lasted for at least several minutes with no clear signals characteristic of the other signals listed – were rare (making up less than 1% of the total eruptive behavior), showing that eruptive activity was consistent and nearly continuous for the duration of the hydrophone deployment. During the 5-month study there was an overall trend of increasing diffuse behavior. In December, at the start of the deployment, diffuse behavior was observed 47% of the time, in contrast with 82% of the time at the end of the study in April. A likely interpretation is that during these 5 months, the eruptive behavior was steadily transitioning from discrete gas slug explosions and effusive behavior to more continuous degassing. One possible explanation for this transition could be if the source of eruptive activity was moving its focus from one eruptive vent (Hades, with explosive gas slugs and effusive activity) to the other eruptive vent (Prometheus, with more continuous degassing).

Selecting signals to use for calculating eruption velocity and cumulative volume

There are two ways in which signals can be altered in their shape and amplitude as multiple raypaths are introduced: reflection off the sea surface, and interference due to multipathing. Modeled raypaths for signals generated at Hades and traveling to each of the four stations were calculated based on standard ocean velocity models from NOAA (figure 4). Raypaths from the south, east, and west stations contain reflected signals, which record a

waveform that no longer accurately represents the physical processes at the vent. For example, at the depth at which the south hydrophone is deployed, a sea surface reflection arrives only 30 ms later than the direct wave. Because many signals representing gas bubble explosions (those below 33 Hz) take longer than 30 ms to complete a cycle, the two signals add together, changing their shape and amplitude. The east and west stations see reflections as early as 20 ms (below 50 Hz), which means that signals seen at these stations will also be "contaminated," and only the first 20 ms of their waveform can be trusted as being a true representation of vent processes. Signal reflections are problematic for data processing, as the signal shape and amplitude are the two most important factors that determine velocity, flux, and volume values. Due to these two possibilities of wave propagation altering the signal, only the first 20 ms of each signal was used for calculations, regardless of what station is being used.

Because wave intensity decays as sound travels from the source, the amplitude of signals at the farthest station (north) should be the smallest, and amplitudes at the closest station (south) should be the greatest of the four stations. However, in most cases amplitudes were observed to be greatest at the north station, presumably a result of constructive wave interference. Because of this, results from calculations at the north station are suspect. Focus is placed instead on results from the south, east, and west stations (i.e., results from the north station are essentially ignored for this study).

Because only the first few ms of the signal are unaffected by multipathing, the diffuse signals could not be used in this study. Diffuse behavior is characterized by continuous degassing at one or both of West Mata's vents. Calculations from these altered signals do not provide an accurate representation of West Mata's true eruption velocity. Vergniolle and

Caplan-Auerbach (2004) provide a method for estimating eruption velocity for diffuse signals assuming a dipole source at the vent. However, their method assumes no signal contamination from secondary arrivals. Thus, the diffuse signals seen at West Mata are unreliable for providing accurate values for calculations used in this study.

Tremor is not believed to be associated with degassing at the vent, but rather with fluid flow within the volcanic conduit (Johnson and Lees, 2000; Lees, Gordeev, and Ripepe, 2004; Fee et al., 2010; Matoza, Fee and Garces, 2010; Jellinek and Bercovici, 2011), and thus tremor is not used in this study.

This leaves the discrete signals, which represent isolated occurrences of gas bubbles rising through magma and bursting upon eruption. There are instances in which discrete signals occur close together (up to 27 events/minute), but even when events are frequent their waveforms are not observed to overlap (figure 17). Therefore, discrete signals were used to constrain values of eruption velocity and cumulative volume.

Time series pre-processing

When data are received on hydrophones, they are recorded in "counts," dimensionless units that record scaled positive and negative pressure changes. However, calculating eruption velocity from acoustic pressure necessitates conversion of amplitudes to units of Pascals. Each hydrophone may not record all frequencies at their true strengths; some will either amplify or dampen certain frequencies or bands of frequencies, making it necessary to bring these recorded frequencies to a level that reflects the original signal. A function written by Del Bohnenstiehl of the University of North Carolina (hydrophone_corr.m; Appendix II)

converts the raw data recorded on the hydrophones from counts to Pascals while correcting for the hydrophone's response.

Because of the extremely large volume of data in this study a goal was to make analysis more expedient by auto-detecting explosion events. However, automation of event detection from the raw data was not possible, because of a very low-frequency (<10 Hz) signal superimposed on a majority of the discrete signals. This signal (which could be made up primarily of tremor) dominated the gas burst signals in many cases (figure 18a). To eliminate this low frequency signal, a 10 Hz highpass filter was applied to the data at West Mata. This enables identification of a greater number of events to be used for velocity and volume calculations (figure 18b).

The signals representing gas bubble bursts at West Mata took up to 100 ms to complete a cycle; these signals contain frequencies above 10 Hz so the filter would not affect signals used for calculations. Also, once the signal is filtered, any offset from being superimposed on a low-frequency background signal is removed, centering the gas bubble burst at zero amplitude (see figure 18). Using these filtered signals for calculations yields more accurate results, because the true amplitudes of the signals are expressed when they are centered at zero Pa. When using the unfiltered data for calculations, many gas bubble burst events are overlooked during event detection (table 1), and velocities change by up to 15% (table 2). Also, because more events are recognized by this algorithm, a larger, and more accurate, cumulative eruption volume is calculated. However, any signals that contain frequencies below 50 Hz would be excluded from calculations because signal reflections limit the duration of the signal to 20 ms.

Before calculating eruption velocity and cumulative volume, events needed to be identified according to certain parameters that define the length of an event and its shape and amplitude relative to the background noise (lta_sta_velflux.m; Appendix II). This was done using a short-term average/long-term average (STA/LTA) method that compares ratios of the root mean square (RMS) signal amplitude of a short time frame to that of a slightly longer time frame. If the ratio of the short-term window (STW) to the long-term window (LTW) exceeds a specified value (hereafter referred to as a detection threshold), a segment of the data is selected as possibly representing a single gas bubble burst (figure 19), depending on its shape and duration (see figures 6, 10, 11). However, signals with any abrupt increase in amplitude – such as earthquakes – may also be chosen by this algorithm. Because of these extra events identified, it became necessary to go through these events by hand and discard those that did not represent gas bubble bursts; this manual step inhibited complete automation of event detection.

STW and LTW values were experimentally varied with the objective of identifying the greatest number of events representing gas bubble bursts (table 3). An optimal detection threshold was chosen with the goal of finding the greatest number of gas burst events while also minimizing the number of signals that do not represent gas explosions. This was carried out on the south station, because its proximity to the sound source decreases the amount of spatiotemporal variability influencing the signal (Fee and Matoza, 2013).

Another requirement for an optimal detection threshold is to find events with the greatest range of amplitudes. When a higher detection threshold is set, it is less likely that the non-events will be included (except earthquakes, whose amplitudes can be significantly larger than those in all other signals), but it also rules out real events with smaller amplitudes.

A lower detection threshold will include both small and larger amplitude events, but it does so at the risk of including more non-events. To select an optimal detection threshold is to compare the ratio of the number of hand-picked events to the number of auto-picked events. Whichever detection threshold has the highest ratio of hand-picked events to auto-picked events is taken to be the optimal detection threshold. Detection thresholds of 1.5, 2.0, 2.5, 3.0 and 3.5 were tested at West Mata. The greatest ratio of real events selected by hand to those automatically chosen was found with a detection threshold of 2.0, so more detailed attention was directed to detection thresholds of 1.8, 1.9, 2.0, 2.1, and 2.2 (table 4). Using these values, several half-hour segments of time were chosen on different days. At least 2 days were chosen from each of the 5 months of hydrophone deployment in order to provide the most accurate representation of changing eruptive behavior. For each half-hour segment using a detection threshold value of 1.8 – 2.2, the number of real events picked by hand was recorded. Out of the eleven time frames used, all of them yielded the greatest number of verifiable events with a detection threshold of 1.8. This is the detection threshold value that was used for identifying events for velocity and volume analysis (table 4). Detection thresholds were also tested from 1.8 down to 1.5. While the number of hand-selected events – determined to be "real" events – increased with each incremental lowering of the detection threshold, the increase in the number of auto-selected events was greater. Therefore, the ratio of hand-selected to auto-selected events decreased below a detection threshold of 1.8. Detection threshold values below 1.8 are not reported in table 4.

An alternate method for estimating the number of explosion events involved the use of b-value. B-value quantifies the number of events greater than a given amplitude, and is expressed as the slope of a plot of signal amplitude versus the log number of events. The b-

value was originally used to study the distribution of earthquake magnitudes worldwide, but it can be applied to any type of event with a power law distribution. In this study, the b-value of explosions at West Mata was calculated (bvalue.m; Appendix II) using the absolute value of the maximum amplitude of the signal in place of the earthquake magnitude (figure 20). Having a consistent b-value in West Mata's data would indicate that no matter what amount of time was used, the distribution of the signal amplitudes would be the same; there would be a constant rate of increase in the number of events seen for each progressive decrease of signal amplitude. For example, if the b-value was 1, the log-linear relationship would indicate that the value representing this constant rate of increase is 10, and there would be 10 times as many events with amplitude 3.0 Pa as 2.0 Pa; 10 times as many events with amplitude 2.0 Pa as 1.0 Pa, etc. (In general, a higher b-value indicates a greater increase in progressively smaller amplitude signals, leaving a greater overall percentage of smaller amplitude events.) If a consistent b-value were to be found in West Mata's data, then it would be easy to estimate the number of explosion events of a given amplitude. From there, the total number of explosion events could be found at West Mata based on the distribution from the b-value. This could be done by finding a high detection threshold for which 100% of the signals chosen by the script are in fact real signals that represent gas bubbles bursting.

The b-value is calculated by first identifying explosions in the time series, and then determining how many events there are equal to or greater than a given amplitude. The amplitudes were set at intervals of 0.1 Pa, and the number of events greater than each amplitude value was recorded. The slope of the line plotted by the log number of events and amplitude is the b-value for that time frame. However, b-values for signal amplitudes at 11 different time frames at West Mata ranged from 0.16 – 0.84 (table 5). This means that some

time frames at West Mata have a distribution of signal amplitudes such that there is a mild increase in the number of events for progressively smaller amplitudes (e.g., b = 0.16), but other time frames contain a significantly larger number of events for each incremental decrease in amplitude (e.g., b = 0.84). Overall, this indicates that the long-term distribution of discrete signal amplitudes varies greatly. Because of these highly inconsistent values, the b-value method could not be used to automatically pick events and extrapolate for the 5-month cumulative flux at West Mata.

Because total automation of calculations was not possible, the best method for calculating total eruptive volume at West Mata during the 5-month deployment was to select events by hand for a portion of the data, and then extrapolate for the number of hours during which discrete events were dominant. Because some time periods had less explosive activity (5 events per minute) and other time periods had more frequent explosions (27 events per minute), it was necessary to account for changing rates of explosivity. This was done by finding the total number of hours of purely discrete activity (see figure 16), and calculating the percentage of times for minimum and maximum explosivity, and extrapolating accordingly.

Eruption velocity and cumulative volume

The method used for calculating the eruption velocity and cumulative volume at West Mata is based on previous studies that use acoustic pressure at subaerial volcanoes to calculate the velocity and volume of volcanic eruptions (Woulff and McGetchin, 1976; Vergniolle et al., 2004; Vergniolle and Caplan-Auerbach, 2004, 2006; Caplan-Auerbach et al., 2010). This study is the first to use this technique in the undersea domain.

Once discrete explosion events were identified, their amplitudes could be related to acoustic power Π according to

$$\prod = \frac{\pi r^2}{\rho_{sw} c \tau} \int_0^{\tau} \left| p - p_{sw} \right|^2 dt$$

(Lighthill, 2001), which relates the acoustic power at a sound source to the overpressure recorded at distance r from the source for a signal with a duration of t. The sound wave emitted from the source will also be affected by properties of the medium through which it travels (including ρ_{sw}, the density of the seawater – 1029 kg/m^3, and c, the speed of sound in seawater – 1495 m/s). The excess pressure, p, is recorded in Pa at the hydrophone relative to the ambient pressure of the seawater, p_{sw}.

Different eruption types generate different amounts of acoustic power. Because the gas bubble explosions used in this study behave as a monopolar source of sound, the acoustic power is related to the fourth power of the velocity (for dipoles, this would be the sixth power of velocity; for quadrupoles, the eighth power; Lighthill, 2001):

$$\prod_m = K_m \frac{4\pi R^2 \rho_{sw} u^4}{c}$$

A greater acoustic power will be generated by a larger radius of the sound source (R). Ken Rubin (pers. comm, 2012) indicates that gas bubbles reached a maximum size of 1 meter in diameter, but Resing et al. (2011) observed bubble diameters to range from 0.25 m – 1.0 m. Thus, in the calculations for this study, a range of values is given based on a range of radii from 0.125 m to 0.5 m. K_m is an empirically derived constant, and is shown to be (1/16) for a circular flat orifice at a monopolar sound source (Vergniolle and Caplan-Auerbach, 2004), such as a volcanic vent. The equation can be rearranged to solve for u, the eruption velocity.

$$u = \sqrt[4]{\frac{\prod_m c}{K_m 4\pi R^2 \rho_{sw}}}$$

Once the eruption velocity (u, in m/s) is determined, the eruptive flux for that gas bubble explosion can easily be calculated. Flux is a measure of the volume of a material erupted per unit time, represented by the product of eruption velocity and the cross-sectional area of the vent. The area through which material is erupting is determined by the diameter of the gas bubble, therefore, flux is calculated as a range of values in accordance with the minimum and maximum bubble dimensions (i.e., area is calculated for a radius of 0.125 m and 0.5 m).

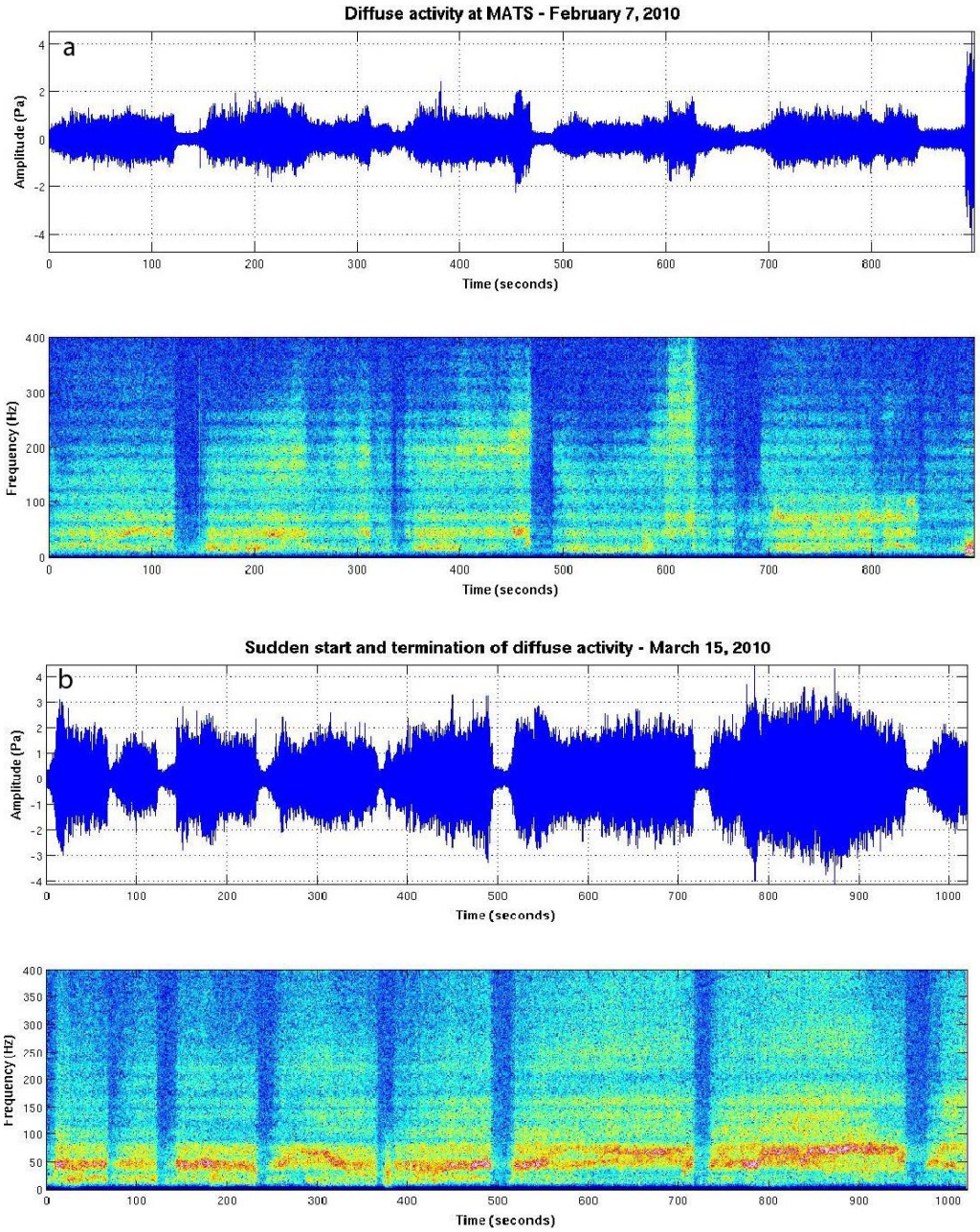

Fig. 12. Diffuse signals (top figure) represent one major type of eruptive activity at West Mata. These signals can start and terminate abruptly (bottom figure), indicating the formation of a magma quench cap on the vent between degassing events. Spectrograms show that energy in diffuse signals can be seen up to 400 Hz. Apparent harmonics with a fundamental frequency of about 30 Hz is believed to be a product of multipathing, with destructive interference creating frequency bands at which it appears there is either very weak or no signal. Note the strong frequency signal (~30-100 Hz) in the bottom figure. Although it is common, this strong frequency signal is not ubiquitious in diffuse signals.

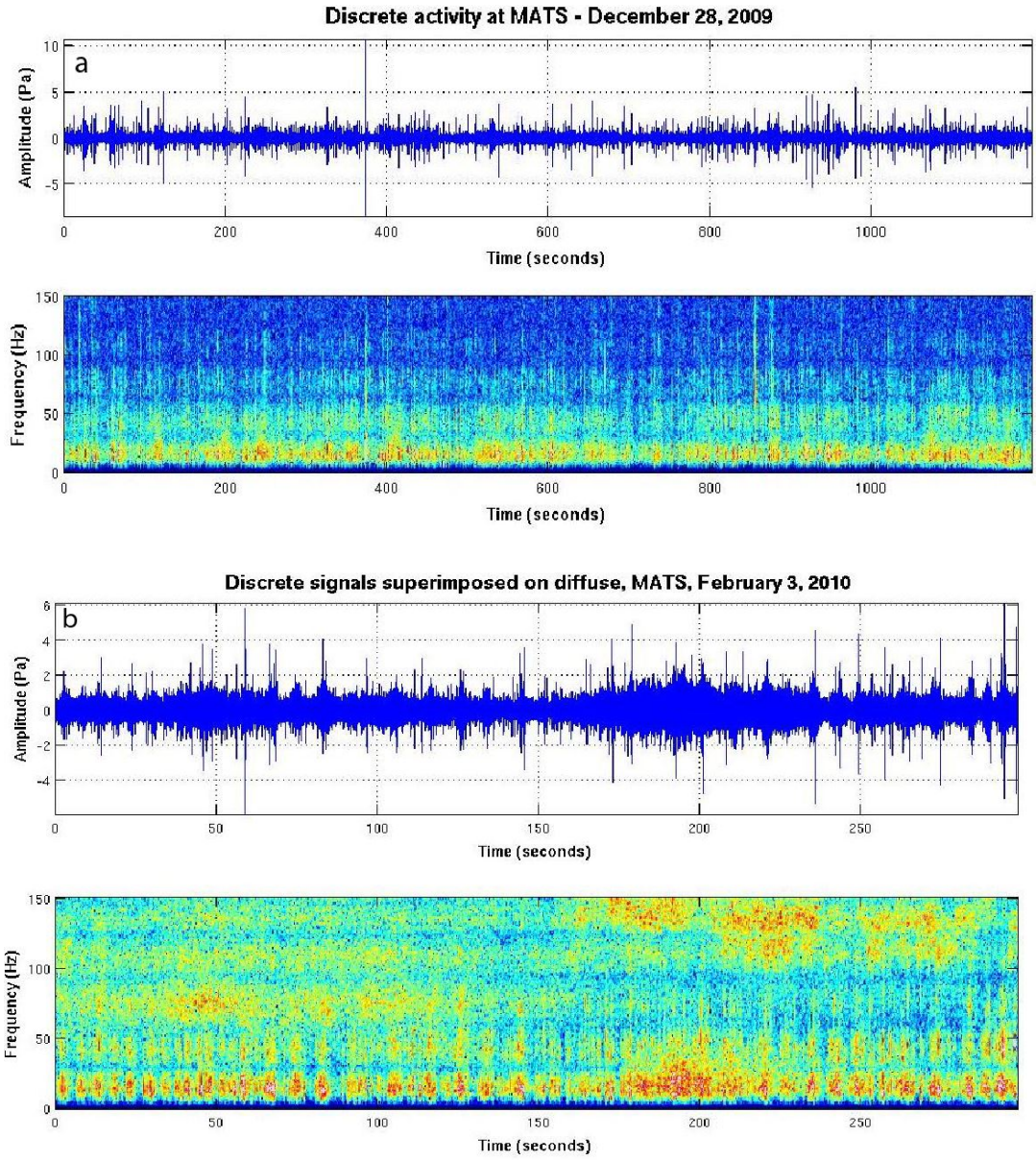

Fig. 13. Example from West Mata of discrete signals (top figure), as well as discrete signals superimposed on diffuse signals (bottom figure). Data have been highpass filtered at 10 Hz. Note that the maximum frequency of the spectrograms above is 150 Hz.

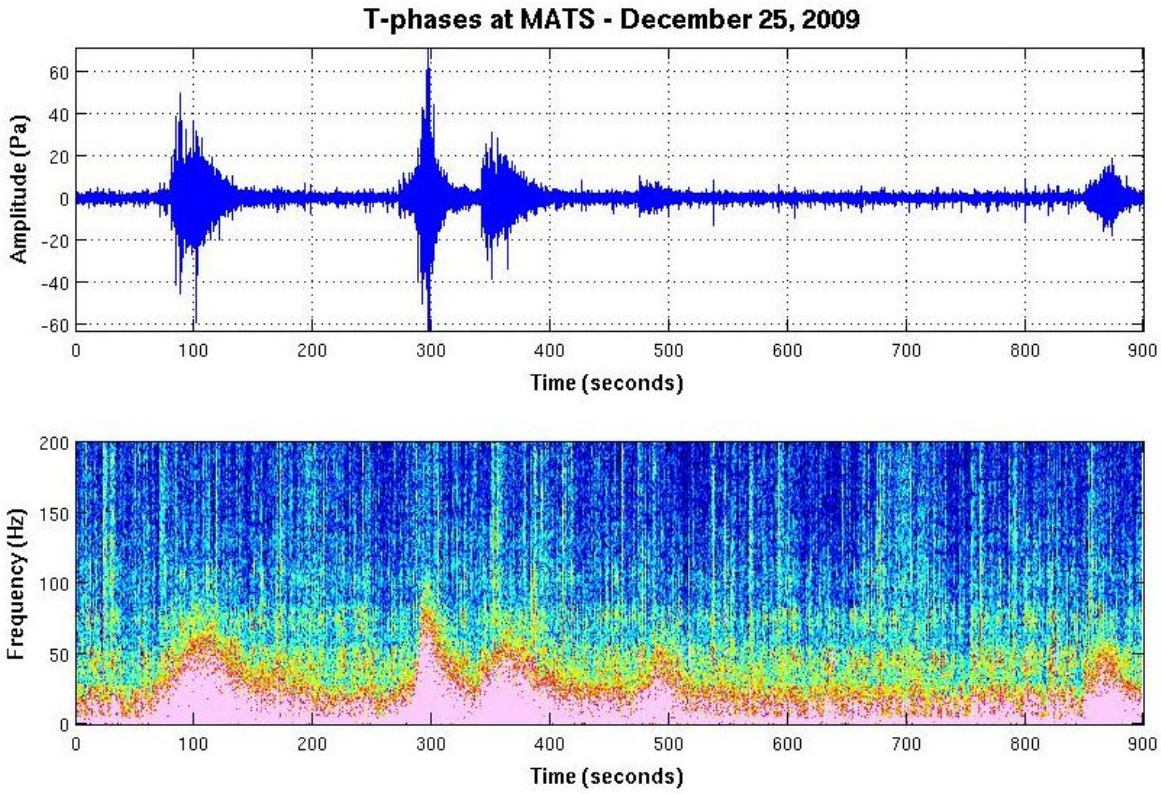

Fig 14. For less than 5% of the 5-month study period, T-phases were a dominant signal. T-phases bear similarity in waveform and spectral content to earthquakes: they have high-amplitudes, are symmetric in waveform, and contain strong low (< ~50 Hz) frequencies.

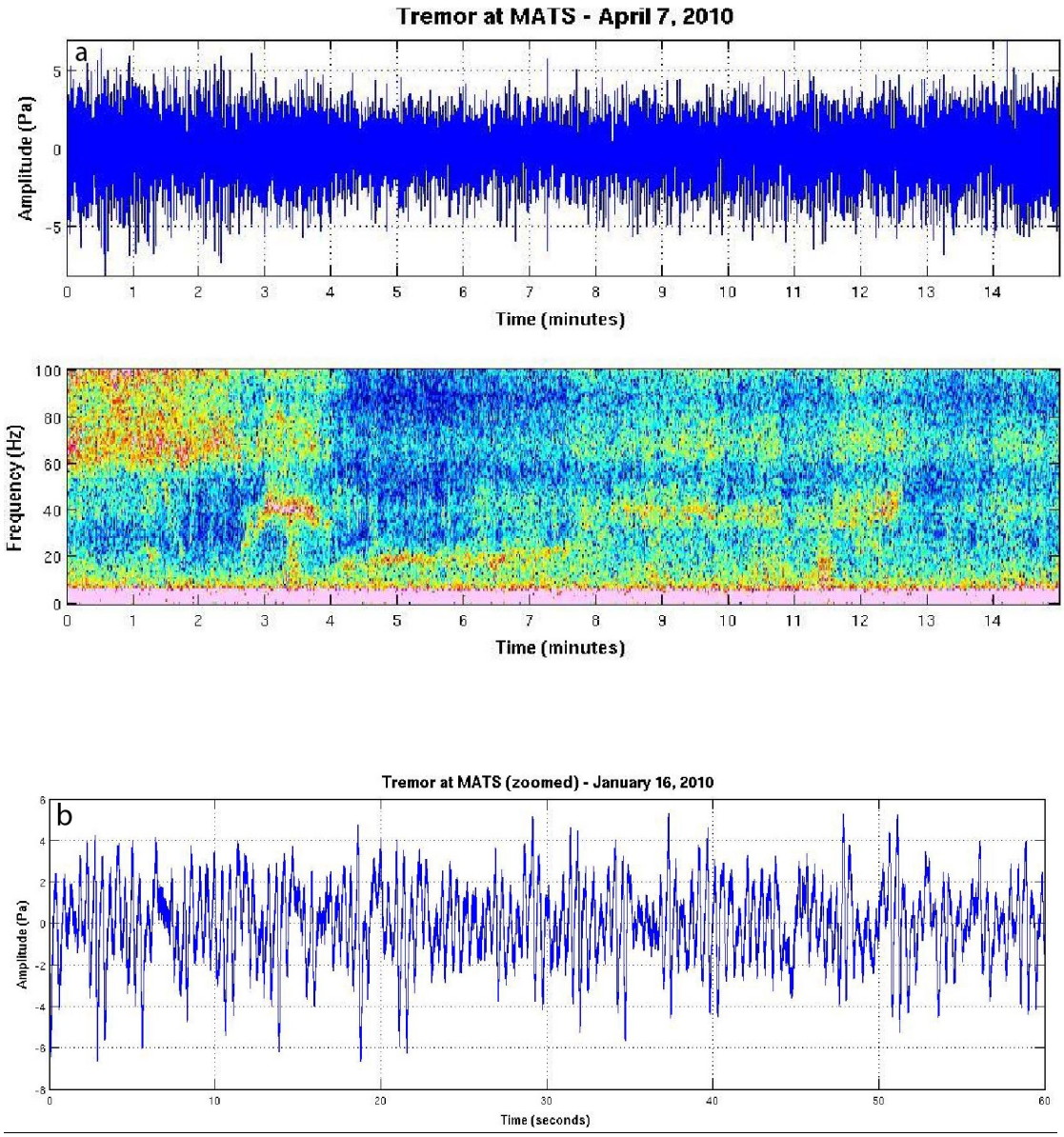

Fig. 15. Tremor seen at West Mata can bear similarity in waveform to diffuse signals, but spectrograms show a strong fundamental frequency < 5 Hz (top figure – note that the maximum frequency shown in the spectrogram is 50 Hz). The bottom figure is a zoomed-in portion (1 minute in length) of the tremor signal from January 16, 2010, which shows an unfiltered signal with asymmetric amplitudes that contains no distinct beginning or end.

Fig. 16. Calendar representing percentage of each signal type per day in December (top) and graphical representation of signal types for all 5 months (bottom). Percentages of each signal type in December are shown in the bottom right corner of the calendar (top). As shown in the bottom figure, there was an overall decrease in the amount of discrete signals seen (pink color), and an increase in the amount of diffuse signals seen (blue color). The amount of T-phase signals remained fairly constant throughout the 5-month study period.

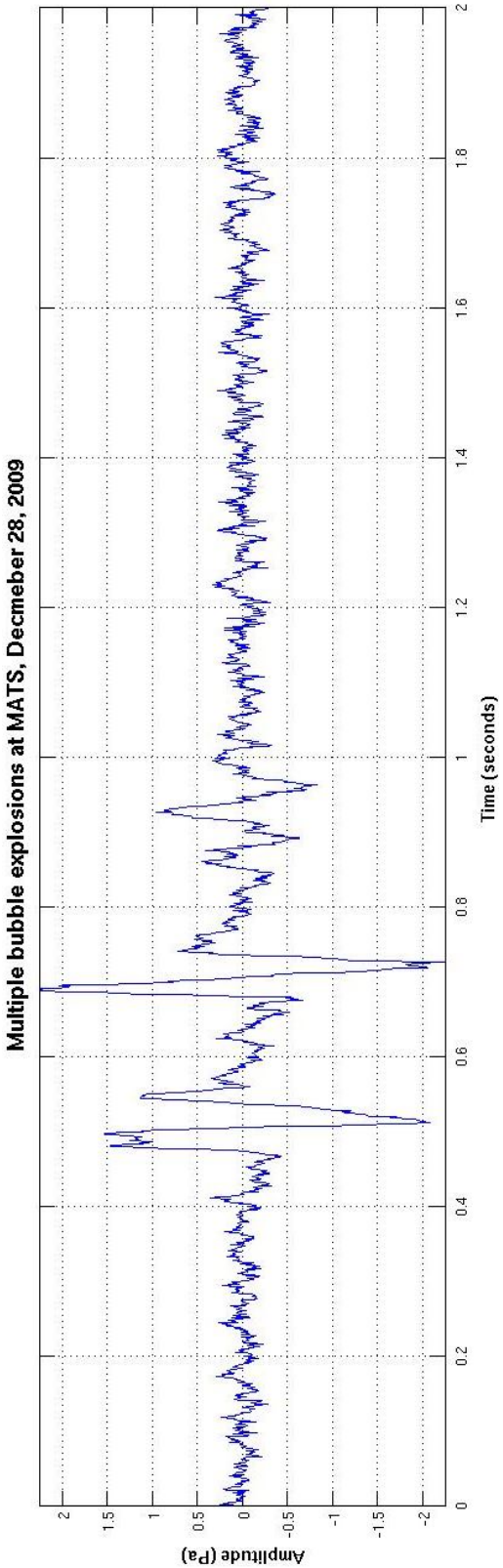

Fig. 17. Discrete signals at West Mata occur as frequently as 5 – 27 events per minute. The figure above shows 3 events in 2 seconds. Because they do not overlap, discrete signals can be used for calculations in this study.

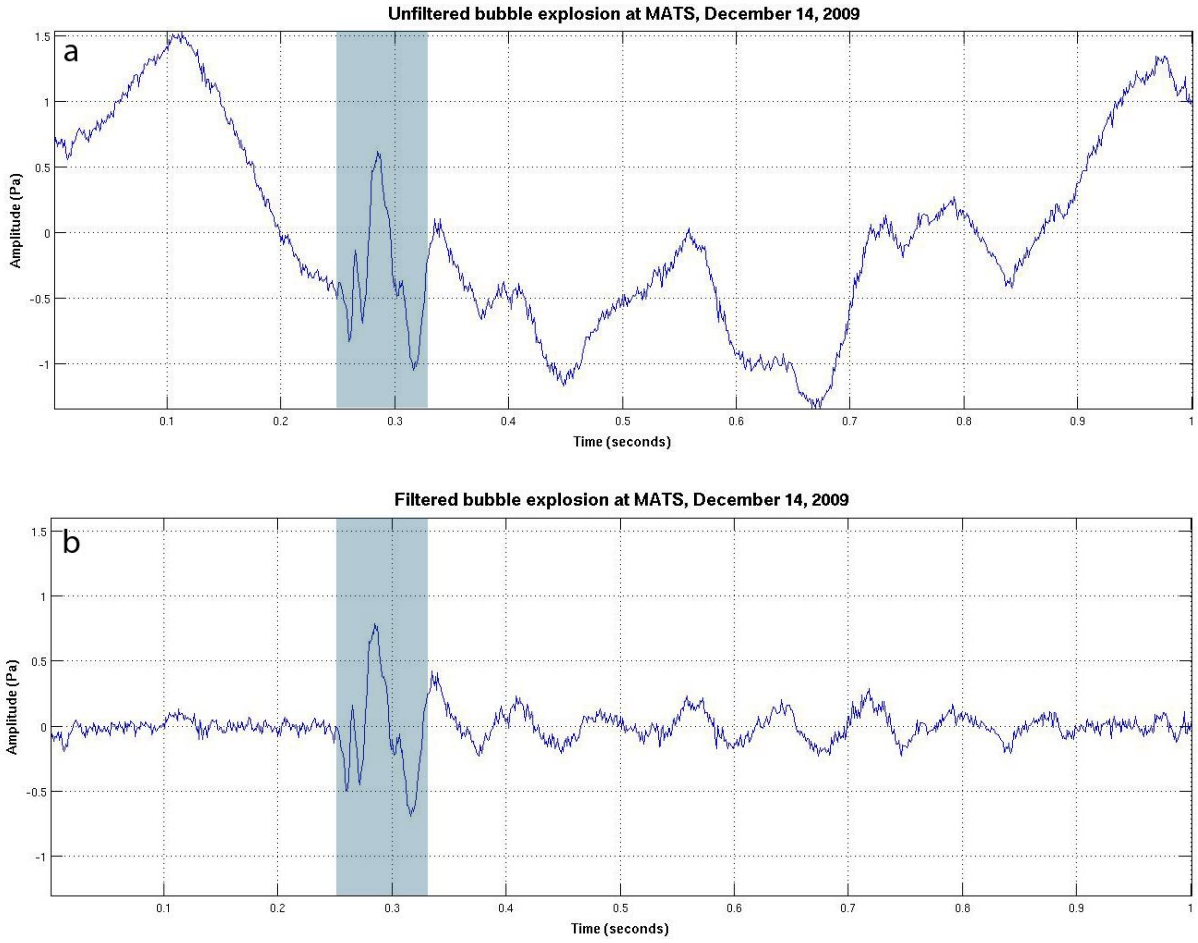

Figure 18. The figures above highlight the same explosion event, both unfiltered (a) and with a 10 Hz highpass filter (b). Note that the signal highlighted above is shown at the same scale in each figure, yet the amplitudes are different; filtering the signal yields a more accurate representation of the amplitudes, as it centers the signal at zero Pa (b), instead of superimposing the signal on a low-frequency background noise (a). Fewer explosion events were selected using unfiltered data than when a 10 Hz highpass filter was applied. This is because the amplitude of the waveform under 10 Hz often was greater than the amplitude of the gas bubble waveform in the unfiltered data (e.g., see figure a). Real events were not guaranteed to be picked in the unfiltered data because of this difference in amplitudes.

YEAR - JULIAN DAY, TIME FRAME	FILTER?	u (RANGE, m/s)	NO. OF EVENTS	RANGE OF FLUX (m^3/s)	CUM. VOL. (m^3)
2009 - 348, 10:10-10:40	10 Hz hp	1.5 - 23.0	280	0.1 - 18.1	1 – 13
	none	1.7 - 26.4	89	0.1 - 20.7	1 – 9
2009 - 356, 01:30-02:00	10 Hz hp	2.0 - 18.4	168	0.1 - 14.5	1 – 13
	none	2.9 - 24.6	75	0.1 - 19.3	1 – 8
2009 - 363, 04:19-04:49	10 Hz hp	1.9 - 17.2	287	0.1 - 13.5	1 – 19
	none	4.1 - 23.2	33	0.2 - 18.2	1 – 4
2010 - 004, 16:05-16:33	10 Hz hp	1.7 - 27.6	154	0.1 - 21.7	1 – 10
	none	2.2 - 29.8	84	0.1 - 23.4	1 – 8
2010 - 018, 17:38-18:07	10 Hz hp	1.4 - 14.2	353	0.1 - 11.2	1 – 16
	none	4.9 - 24.0	9	0.2 - 18.9	0 – 1
2010 - 043, 01:35-02:04	10 Hz hp	2.1 - 23.8	328	0.1 - 18.7	1 – 22
	none	1.7 - 24.2	150	0.1 - 19.0	1 – 13
2010 - 049, 15:49-16:18	10 Hz hp	1.6 - 18.0	748	0.1 - 14.1	2 – 40
	none	1.5 - 20.3	310	0.1 – 16.0	1 – 22
2010 - 062, 20:29-20:58	10 Hz hp	3.3 - 21.0	292	0.2 - 16.5	2 – 25
	none	2.7 - 28.4	214	0.1 - 22.3	1 – 22
2010 - 093, 02:59-03:28	10 Hz hp	1.9 - 30.4	240	0.1 - 23.9	1 – 20
	none	2.3 - 31.0	57	0.1 - 24.4	1 - 6

Table 1. The number of events and the range of eruption velocity (u), cumulative flux, and cumulative volume were compared for nine different half-hour segments of time on nine different days, using a detection threshold of 2.0. Numbers are shown above. Note that a 10 Hz highpass filter selects more events, which leads to a greater cumulative flux for each time frame. The 10 Hz highpass filter also removes the long-period signal that offsets explosion events from zero, resulting in a more accurate representation of the apparent amplitudes of each explosion event. Thus, we believe the cumulative flux to be more accurate when a 10 Hz highpass filter is used.

FILTER	u (range, m/s)	MAX AMPLITUDE (range, Pa)	FLUX (range, m^3/s)
None	2.4 - 22.8	0.67 - 9.35	0.2 - 17.9
10 Hz hp	2.6 - 19.2	0.46 - 8.24	0.1 - 15.1

Table 2. This table shows the difference between filtered and non-filtered events on the South station for the 36 West Mata events representing a range of amplitudes, durations, and frequencies. For each of the 36 events, the range of velocities were calculated, as well as the ranges of the max amplitude and instantaneous flux. Even though the range of values for velocity is greater when the filter is applied to the data, the results in Table 1 show that using the 10 Hz hp filter selects many more events, yielding a more accurate cumulative eruptive volume.

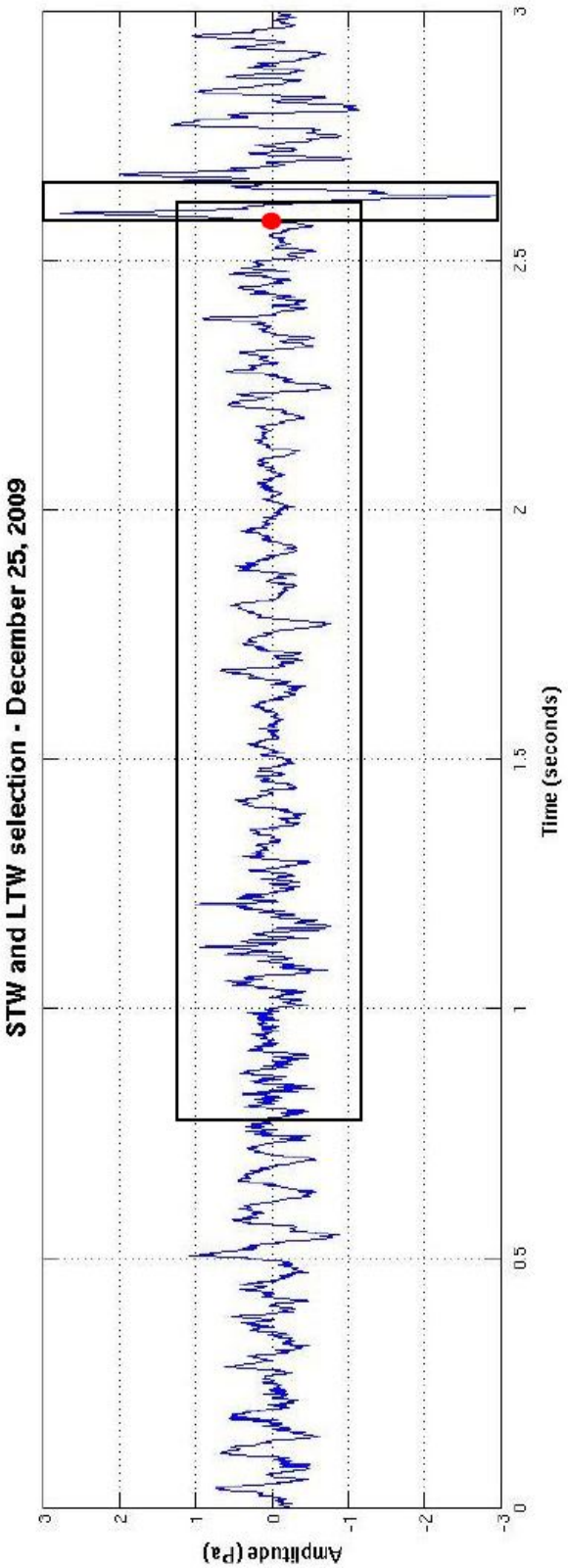

Fig. 19. Figure from Julian Day 359 (December 25, 2009) illustrating the selection of an event using the STA/LTA algorithm. In this image a short-term window (0.1 seconds, box on right) and a long-term window (2 seconds, box on left) are shown in black boxes. For a waveform to be selected, the ratio of the RMS amplitude of the short-term window relative to that of the long-term window must exceed an established detection threshold. The red dot signifies the spot at which the script recognizes an event, if

YEAR - JULIAN DAY, TIME FRAME	STW: 0.1 LTW:2.0	STW: 0.08 LTW: 2.0	STW: 0.1 LTW: 1.5	STW: 0.12 LTW: 2.0
2009 - 363, 04:19 - 04:49	**293**	206	187	172
2010 - 004, 16:05 - 16:33	**206**	161	108	133
2010 - 043, 01:35 - 02:04	**408**	280	287	283
2010 - 062, 20:29 - 20:58	348	**370**	341	227
2010 - 093, 02:59 - 03:28	**183**	175	107	129

Table 3. Short term window (stw) and long term window (ltw) values were experimentally derived to find the best settings. One day from each month of the study was selected. Results were based on the stw and ltw values that yielded the greatest number of events at a detection threshold of 1.8, which was found to be the most optimal detection threshold for hand-picking events. The best stw and ltw values were found to be 0.1 and 2.0 seconds, respectively. Boldfaced numbers indicated the greatest number of events selected for that time frame.

Table 4a

YEAR - JULIAN DAY, TIME FRAME	(# HAND-SELECTED EVENTS)/(# AUTO-IDENTIFIED EVENTS)	DETECTION THRESHOLD	RANGE OF FLUX (m^3/s)	CUM. VOL (m^3)
2009 - 348, 10:10-10:40	**374/743**	1.8	**0.07 - 18.69**	**1.1 - 17.5**
	342/617	1.9	0.07 - 21.05	1.0 - 16.5
	280/521	2	0.07 - 18.06	0.8 - 13.4
	232/438	2.1	0.08 - 17.59	0.7 - 11.5
	241/374	2.2	0.08 - 20.26	0.7 - 11.7
2009 - 356, 01:30-02:00	**470/897**	1.8	**0.07 - 14.29**	**1.9 - 29.7**
	296/747	1.9	0.10 - 14.45	1.3 - 20.3
	168/625	2	0.10 - 14.45	0.8 - 12.8
	152/531	2.1	0.10 - 14.45	0.7 - 11.9
	150/452	2.2	0.12 - 14.45	0.7 - 11.55
2009 - 363, 04:19-04:49	**424/576**	1.8	**0.08 - 13.51**	**1.7 - 26.6**
	366/484	1.9	0.10 - 16.96	1.5 - 23.9
	287/426	2	0.09 - 13.51	1.2 - 19.3
	199/364	2.1	0.14 - 13.51	0.9 - 14.5
	170/320	2.2	0.12 - 13.35	0.8 - 12.3
2010 - 004, 16:05-16:33	**206/720**	1.8	**0.07 - 21.36**	**0.8 - 13.2**
	165/603	1.9	0.07 - 12.10	0.7 - 10.6
	154/508	2	0.08 - 21.68	0.6 - 10.2
	138/423	2.1	0.08 - 21.68	0.6 - 9.5
	130/374	2.2	0.08 - 20.73	0.6 - 9.0
2010 - 018, 17:38-18:07	**405/1102**	1.8	**0.05 - 11.31**	**1.1 - 17.6**
	341/913	1.9	0.07 - 10.68	1.0 - 15.6
	353/773	2	0.07 - 11.15	1.0 - 16.0
	303/638	2.1	0.06 - 11.31	0.9 - 14.0
	360/528	2.2	0.07 - 11.31	1.0 - 16.4
2010 - 043, 01:35-02:04	**408/887**	1.8	**0.10 - 18.69**	**1.6 - 26.1**
	297/737	1.9	0.10 - 18.69	1.2 - 19.4
	328/613	2	0.10 - 18.69	1.4 - 21.7
	244/509	2.1	0.10 - 18.54	1.0 - 16.4
	209/421	2.2	0.10 - 18.69	0.9 - 14.6
2010 - 049, 15:49-16:18	**748/1135**	1.8	**0.08 - 14.14**	**2.8 - 45.1**
	666/983	1.9	0.08 - 12.57	2.5 - 39.6
	654/878	2	0.08 - 14.14	2.5 - 39.7
	548/779	2.1	0.07 - 12.10	2.1 - 33.7
	502/690	2.2	0.008 - 12.57	1.9 - 30.2

Table 4b				
YEAR - JULIAN DAY, TIME FRAME	**(# HAND-SELECTED EVENTS)/(# AUTO-IDENTIFIED EVENTS)**	**DETECTION THRESHOLD**	**RANGE OF FLUX (m^3/s)**	**CUM. VOL (m^3)**
2010 - 062, 20:29-20:58	**329/976**	1.8	**0.12 - 16.81**	**1.7 - 27.8**
	291/774	1.9	0.13 - 16.34	1.6 - 25.4
	292/614	2	0.16 - 16.49	1.6 - 25.4
	231/497	2.1	0.14 - 16.65	1.3 - 20.5
	205/418	2.2	0.17 - 16.65	1.2 - 18.9
2010 - 073, 15:05-15:34	**539/1314**	1.8	**0.10 - 13.98**	**2.4 - 39.0**
	415/1138	1.9	0.09 - 17.28	1.9 - 29.9
	424/972	2	0.09 - 15.24	1.9 - 30.8
	404/837	2.1	0.10 - 17.28	1.8 - 29.4
	355/724	2.2	0.10 - 14.29	1.6 - 25.9
2010 - 093, 02:59-03:28	**568/1232**	1.8	**0.07 - 24.19**	**2.7 - 43.2**
	481/1068	1.9	0.07 - 24.19	2.4 - 37.7
	240/911	2	0.09 - 23.88	1.3 - 20.3
	144/758	2.1	0.11 - 24.19	0.8 - 12.4
	122/651	2.2	0.11 - 23.40	0.6 - 10.4
2010 - 101, 04:00-04:29	**801/1384**	1.8	**0.06 - 14.45**	**3.2 - 51.4**
	449/1211	1.9	0.07 - 16.49	1.9 - 29.8
	340/1068	2	0.10 - 16.34	1.5 - 24.1
	313/920	2.1	0.09 - 15.87	1.4 - 21.9
	263/800	2.2	0.09 - 16.49	1.2 - 18.9

Table 4. Results from the investigation to find the optimum detection threshold based on the greatest number of hand-selected events, using values of 1.8, 1.9, 2.0, 2.1, and 2.2. The number of events and cumulative flux were generated for the same half-hour time segments as listed in table 1. Bold numbers indicate the values for which the greatest number of automatically detected events were considered "real." This was consistently found at a detection threshold of 1.8. A detection threshold of 1.8 was therefore used for calculating cumulative eruptive flux at West Mata, using the method of hand-selecting events and extrapolating for cumulative volume for the entire eruption.

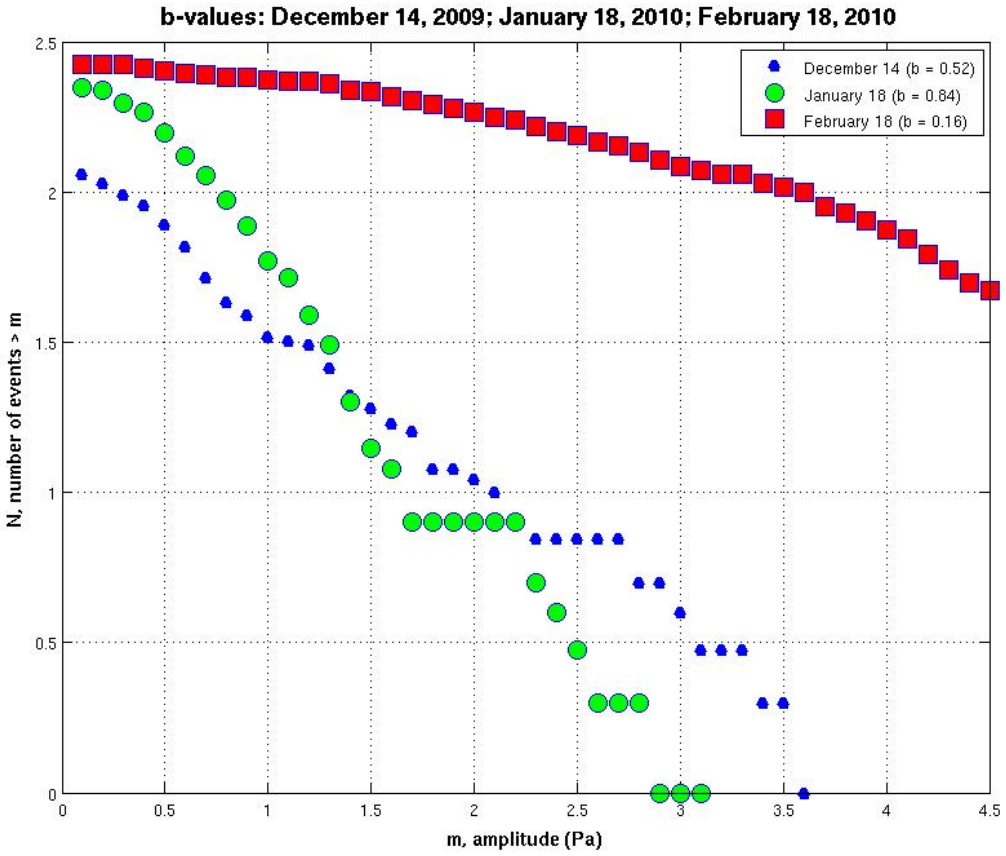

Fig. 20. Example of a frequency-magnitude plot from West Mata data showing the b-value for 30-60 minute time segments on three different days, representing the minimum and maximum b-values seen at West Mata, as well as an intermediate b-value. B-values at West Mata ranged from 0.16 – 0.84 over eleven different days, suggesting that b-value is not a viable method for calculating eruptive flux at West Mata.

JULIAN DAY/TIME FRAME	NUMBER OF HOURS	b-VALUES (RANGE)
(2009) 348, 10:10 - 18:52	7.0	0.43 - 0.64
(2009) 356, 01:30 - 02:11	1.0	0.44 - 0.46
(2010) 004, 16:05 - 17:03	1.0	0.44 - 0.47
(2010) 016, 00:03 - 05:02	2.5	0.23 - 0.30
(2010) 018, 17:38 - 20:37	3.0	0.68 - 0.84
(2010) 043, 00:35 - 04:03	3.0	0.24 - 0.71
(2010) 045, 00:00 - 08:00	8.0	0.22 - 0.36
(2010) 046, 13:03 - 16:02	3.0	0.25 - 0.36
(2010) 049, 11:25 - 17:48	3.0	0.16 - 0.67
(2010) 060, 04:25 - 07:54	3.5	0.25 - 0.39
TOTAL RANGE OF b-VALUES: 0.16 - 0.84		

Table 5. Range of b-values for ten different days at West Mata. Note that the amount of time studied on each day is different, and that there is no pattern of b-values according to the amount of time studied. Because we found the total range of b-values to be quite large for these ten days, we found this method to be unreliable for estimating the cumulative flux at West Mata.

V. Eruption Velocity, Flux, and Volume: Results

Calculating eruption velocity and cumulative volume from acoustic pressure

Using the method described in the previous section, eruption velocities and flux were calculated for 36 representative discrete signals at all four stations surrounding West Mata. These signals span a wide range of frequencies/durations and maximum amplitudes, and are representative of the range seen in discrete signals seen throughout the data. The instantaneous eruption velocity, instantaneous flux, and cumulative volume were calculated for 36 discrete events found on all four stations (table 6); maximum amplitude was also recorded. These events were identified in the time series with the aid of spectrograms (cm_mata_spec.m; Appendix II). Some of these discrete events had very small amplitudes compared to background noise, and thus the spectrograms highlighted and confirmed when each of these signals occurred on each station. In many cases, only two or three stations would clearly display the signal in the time series and/or spectrogram, but the signal would blend into background noise on the remaining stations. Signals were not chosen for calculations unless they were clearly identifiable on all four stations.

The range of eruptive velocities (in m/s) for these 36 events was found to be 2.6 – 19.2 for the south station, 3.1 – 24.6 for the east station, 2.4 – 24.8 for the west station, and 6.3 – 74.4 for the north station (table 6). The significantly higher values calculated for the north station are believed to be due to signal amplification resulting from multipathing. Because of this, reliability of the method was instead evaluated based on the agreement in results from the south, east, and west stations only (i.e., complications from multipathing at the north station led me to exclude results from the north station when considering how well

this method works for the submarine environment). Since eruptive velocities for these three closer stations are of the same order of magnitude, this suggests that the method of using acoustic pressure to calculate eruption velocity in the submarine environment should yield consistent values for a network of stations placed at different distances from the sound source. However, signal multipathing that leads to altered signals (either by constructive or destructive interference) decreases the accuracy of calculated eruptive velocities, as it can potentially limit the duration of the signal used.

These values can be compared with eruptive velocities seen in the subaerial environment. Because of hydrostatic pressure at West Mata's summit (approximately 120 bars for 1200 m depth; compated to 1 bar at sea level), velocities in the submarine enviroment should be expected to be lower than those seen in the subaerial environment. Vergniolle and Brandeis (1996) reported a maximum radial velocity of gas bubbles at Stromboli to be 8 – 60 m/s, assuming a hemispherical cap of lava (similar to the scenario assumed in this study for bursting gas bubbles). Vergniolle et al. (2004) also estimate gas velocity at Shishaldin to be 30 – 60 m/s. Ignoring the north station, values from subaerial studies are up to an order of magnitude larger than those seen at West Mata, as expected. The hydrostatic pressure in the submarine environment likely limits the velocity of escaping gases at West Mata, which could explain why the submarine velocities are an order of magnitude smaller than those seen in the subaerial environment. Since eruption velocity and the degree of volcano explosivity are directly related to the gas content of the magma, the increase in hydrostatic pressure may play only a partial role in affecting the eruption velocity differences between the submarine and subaerial environments.

To calculate eruptive flux, the velocity (in m/s) was multiplied by the cross-sectional area of the volcanic vent (0.20 m^2 for a vent diameter of 0.25 m, to represent smaller gas bubbles bursting, or 0.79 m^2, assuming a vent diameter of 1 m for larger gas bubbles). Eruptive flux for the events mentioned above is estimated to range from 1.9 – 9.7 m^3/s for the south, east and west stations, and 5.0 – 29.2 m^3/s for the north station (table 6).

Eruptive flux can be used to estimate the total volume of erupted material generated by discrete events during the 5-month study at West Mata. To accomplish this, flux (both lava and gas, in m^3/s) is multiplied by the duration of each event (20 ms) to find the volume of each individual event. This can then be multiplied by the estimated total number of explosion events during the deployment. For the 36 events selected, the range of volumes per event at each station (in m^3) is 0.03 – 0.15 for the south station, east and west stations. The cumulative volumes (both lava and gas) for these 36 events at these three stations range from 0.2 – 3.5 m^3 (table 6).

Long-term cumulative eruptive volume at West Mata must be calculated by hand-picking events for a portion of the 5 months of data and extrapolating for cumulative volume expected during those 5 months. This was done by extrapolating for the total number of hours of purely discrete activity in the data from the half-hour segments chosen. The cumulative volumes (lava and gas) for the 11 half-hour segments of time were added together based on the range of eruption velocities and range of vent diameters (see table 7), yielding 21 - 337 m^3 for 5.5 hours. Given a total of 580 hours of discrete activity, and assuming that the cumulative volume for the 5.5 hours is a representative average, the total cumulative eruptive volume of both lava and gas is 2.2 x 10^3 – 3.6 x 10^4 m^3 for discrete activity during the 5-month hydrophone deployment. This translates to an eruption flux of 5.7 x 10^3 – 9.1 x

10^4 m^3/year. Because evidence shows that the eruption intensity at West Mata was at a maximum during this study period (Dziak, in press), the range of yearly eruptive flux calculated here is likely a maximum value possible for discrete events only. During other years when eruptive behavior is less energetic, West Mata's yearly flux rate from discrete events should be expected to be lower than the values given above. However, it is worth pointing out that the discrete events make up less than 50% of the eruption, and any yearly flux estimates given from this study are still an underestimate of the total volumetric change from eruptive activity at West Mata, regardless of the overall eruption intensity.

These values of flux and volume include both gas and lava. However, the percentages of lava and gas can be estimated based on size of ejecta. Using the maximum clast size from ejecta at Prometheus vent (Merle, 2012), which was approximately 8 cm, and assuming a maximum bubble diameter of 1.0 m (Resing et al, 2009; Rubin, pers. comm., 2012), the volume of lava and gas was calculated from a hemispherically shaped bubble with an outer hemispherical layer of 8-cm-thick lava. Because an 8-cm thick rind of lava is unreasonably large for bubbles of 0.25 m in diameter, confirmation from video footage during the 2009 cruise was needed to constrain this thickness. Thus, volume calculations of a 0.25 m diameter bubble use 1.0 cm thickness for the lava rind. Volumetrically, this translates to approximately 22% lava and 78% (expanded) gas for a bubble 1.0 m in diameter, and 41% lava and 59% (expanded) gas for a 0.25 m diameter bubble. However, this is a maximum estimate for lava volume, because it assumes the lava is not vesicular. Merle (2012) report that the tephra samples gathered from Prometheus vent were approximately 25% vesicular. This slightly lowers the lava volumes, with 17% - 31% lava for a range of bubble diameter sizes. Therefore, if the yearly eruptive volume of vesicular

lava only is calculated at West Mata (which is 36% of the total volume), the range becomes 9.6×10^2 - 2.8×10^4 m^3/year. However, because a lower detection threshold (e.g., 1.5) will select up to twice as many events as the selected detection threshold (1.8) for this study, the range of yearly eruptive volume of vesicular magma at West Mata is $1.9 \times 10^3 – 5.6 \times 10^4$ m^3/yr.

In this study eruptive volumes are calculated only for discrete signals (associated with gas bubble bursts), and not diffuse (associated with continuous degassing). Thus the results for flux and volume only account for 37% of the total eruptive duration at West Mata, and it is not known how much volume is represented by diffuse signals (which represent effusive activity). The gas to lava ratio is also an unknown for these diffuse signals. Because only one signal type can be used to calculate eruption velocity, flux, and volume, the volumes presented above are clearly smaller than the actual total volume of lava erupted at West Mata during the 5-month study period.

Comparisons with previous studies

Results from this study were compared to other studies of eruption velocity and volume. In addition, eruptive volumes from another similar submarine volcano – NW Rota-1 in the Mariana Arc – are also discussed below.

Comparison to velocities from video imagery

Calculated eruption velocities were compared with data from two videos recorded during the West Mata eruption. Ken Rubin from the University of Hawaii provided a frame-by-frame sequence video of West Mata eruptions recorded in 2009 (Frame_by_frame;

Appendix I). Each frame in the video is an instantaneous snapshot taken at intervals of 0.13 seconds, and one can determine how many frames it takes for the bubble to grow to its maximum size before bursting. The maximum bubble size was assumed to be 1 meter in diameter, but because the video is zoomed in and exact scale is not known, it is possible that this estimate of size is off by about 50%, making the maximum bubble diameter anywhere between 0.5 – 1.5 meters (Rubin, pers. comm., 2012). The maximum size of the bubble (0.5 – 1.5 meters) was divided by the time it took to grow (5 frames, or 0.65 seconds), yielding an average eruption velocity of 0.8 – 2.3 m/s for this single gas bubble. Because Resing et al. (2011) observed gas bubble diameters to range from 0.25 m – 1.0 m, the range of eruptive velocities for these bubble dimensions were also calculated, giving a range of 0.4 – 1.5 m/s. To keep comparisons between methods consistent, the eruptive values from Rubin's video based on a bubble diameter of 0.25 – 1.0 m will be used.

These end member values of eruption velocity for this gas bubble are up to an order of magnitude smaller than the velocities that were calculated by hand for the 36 events using acoustic pressure (see table 6). Because this is based on comparison with only one magma bubble, one explanation is that the bubble in this frame-by-frame video represents an end member value of eruption velocity (i.e, it is one of the slower bubbles). Another explanation is that the 36 bubbles used for calculations could be smaller than 1.0 m in diameter, which would mean that their velocities would be faster (assuming that the power is the same for two bubbles of differing diameters, the velocity would be higher for a smaller bubble; see discussion at the end of section IV). Because Ken Rubin's frame-by-frame video only contains one gas bubble, it cannot be assumed that it is representative of all gas bubbles for the duration of the study. Furthermore, Rubin estimated this particular bubble to reach 1.0 m

in diameter, so its eruptive velocity can only be compared to larger (1.0 m diameter) gas bubbles seen at West Mata. It is therefore necessary to use additional methods to compare the results of this study to more observed gas bubbles.

A second video used to estimate eruption velocity was provided by Joseph Resing of NOAA. This video consists of a 45-second clip of several bubbles exploding through time at West Mata's Hades vent (45_seconds_degassing; 18_bubbles_WM; Appendix I). Using iMovie, the video was slowed down to 1/8 of its original speed. At a slower speed, I could easily determine exactly when each of the 18 different gas bubbles began to grow and when they reached maximum size before bursting (accuracy of the time taken for the bubble to reach maximum size is known to one decimal place). A range of instantaneous eruptive velocities from this video were calculated using the same method as the previous video (dividing the maximum bubble size by the time it took each gas bubble to grow and burst).

The total range of instantaneous eruption velocities for these 18 bubbles was 0.2 – 5.3 m/s (table 8). These smallest values are also up to an order of magnitude different from those calculated in this study. However, even with a greater difference in the largest velocities, there is still overlap between values from the video imagery and from using acoustic pressure. Therefore, the velocity values compared using these two methods are considered to agree well, which suggests that pressure derived from hydroacoustic signals can be used to accurately estimate eruption velocity at submarine volcanoes.

Even with Dziak's observation of increased eruption intensity during the rapid response cruise, it is important to point out that these videos were not recorded at the same time as the hydroacoustic data were gathered, and thus the two techniques of calculating eruption velocity cannot be directly compared. This suggests that using hydroacoustic data

to estimate eruption velocity for the submarine environment may be a viable method, but because of the variation in eruption intensity over short time periods (Rubin, pers. comm., 2012), it is difficult to constrain eruption velocities to a narrow range of values, or to expect velocities to stay within the same order of magnitude for the duration of the eruption. However, considering that these two techniques produced comparable results for two different time frames, it suggests that these methods might be applicable to the submarine environment..

Comparison to long-term volume change at West Mata

Clague et al. (2011) estimated the long-term change in volume at West Mata from bathymetric surveys spanning 14 years. Depth differences around the volcano (up to approximately 96 m depth) were noted between the first and last studies, and could be translated into a total positive volumetric increase during the study period. These values represent the addition of material from eruptive activity, and do not include gas volume. For the 14-year period, Clague et al. (2011) calculated a total volumetric increase of 8.0×10^7 m^3, for an average of 5.7×10^6 m^3/yr..

Yearly eruptive volume rates from this study (described above) from only vesicular lava are $1.9 \times 10^3 – 5.6 \times 10^4$ m^3/yr (using a detection threshold of 1.5 to select events). These results suggest a lower eruptive volume estimate (two to three orders of magnitude smaller) than that given by Clague et al.'s yearly volumetric estimates. However, the signals selected for calculations in this study only include one eruptive style, and cover approximately one third of the time during the 5-month study period. Because it is not known how much eruptive volume is overlooked from the diffuse signals, the results from

this study are minimum values and cumulative volume estimates will necessarily be lower than those given by Clague et al., whose bathymetric surveys cover magmatic output from all volcanic behaviors. Therefore, this method is viable for calculating minimum values for the submarine environment.

Comparison to NW Rota-1 volcano

NW Rota-1 is a submarine volcano in the Marianas arc that is in many ways similar to West Mata. Both volcanoes have steep-sided conical shapes, and exhibit both explosive and effusive activity for prolonged time periods (minutes to hours). Chadwick et al. (2008b) note that NW Rota-1's behavior evolved from effusive to explosive over a seven-day observational period. Both volcanoes exhibit rhythmic eruptive bursts that display variations in intensity and are classified as submarine Strombolian (Chadwick et al., 2008b; Walker et al., 2008; Clague et al., 2011; Resing et al., 2011).

NW Rota-1's summit is at a depth of 520 m. West Mata's summit is at a depth of 1200 m, resulting in a higher hydrostatic pressure at its summit (approximately 120 bars at West Mata's summit, compared to approximately 50 bars at NW Rota-1), but the two volcanoes are similar enough in eruptive behavior that their eruption velocities and cumulative volumes can be compared. Overall, explosion intensities (i.e., signal amplitude) at NW Rota-1 are known to vary over several orders of magnitude (Chadwick et al., 2008b; Dziak et al., 2009; Dziak et al., 2012). Chadwick et al. (2008b) conducted bathymetric surveys of NW Rota-1's flanks to estimate the total volumetric change over a 3-year period from 2004 – 2006. This analysis yields a volumetric flux rate (lava only) of 10-100 m^3/hr at NW Rota-1 volcano, which means that the average yearly volumetric flux is approximately

$8.8 \times 10^5 – 8.8 \times 10^6$ m^3. Walker et al. (2008) conducted a 4-year bathymetric survey to determine eruptive volume changes at NW Rota-1 between 2003 – 2006, giving an average annual magmatic flux of 8.3×10^6 m^3/yr, which is in very close agreement with values from Chadwick et al.'s (2008b) results. Table 9 shows all eruption velocity and flux values calculated by the method presented in this study, alternative methods for West Mata, and also numbers from NW Rota-1.

Both Chadwick et al.'s (2008b) and Walker et al.'s (2008) yearly eruptive volumetric rates at NW Rota-1 agree well with Clague et al.'s (2011) yearly eruptive volume changes seen at West Mata, despite the fact that each of these studies span a different number of years. This suggests two volcanoes were exhibiting similar eruptive rates during the study periods. As mentioned above, because the data from the 5-month study period at West Mata (December 2009 – January 2010) can only use discrete signals for calculations, the yearly eruptive volumes excluding gas ($1.9 \times 10^3 – 5.6 \times 10^4$ m^3/yr) are expected to be lower than those given by Clague et al. (2011) at West Mata, and those given by Chadwick et al. (2008b) and Walker et al. (2008) at NW Rota-1. This supports the above conclusion that the results from this study do provide plausible minimum values, and that this method can be used with that in mind for other volcanoes in the submarine environment.

Further studies using hydroacoustic data with simultaneous video recordings are needed to accurately constrain the yearly eruptive volume rate seen at West Mata. The hydrophone setup should eliminate signal reflections from multipathing, so that a method could also be developed to estimate eruption velocity and volume for diffuse signals, yielding more accurate values for the cumulative eruptive flux at West Mata. Using these data without sea surface reflections could also prove how accurate this method is for the

submarine environment, and whether or not more studies should seek to employ this method in adding understanding to submarine volcanoes.

STATION	ERUPTION VELOCITY (range, m/s)	MAX AMPLITUDE (range, Pa)	FLUX (range, m^3/s)	VOUME PER EVENT (range, m^3)	CUMULATIVE VOLUME (m^3)
SOUTH	2.6 - 19.2	0.46 - 8.24	2.0 - 7.5	0.03 - 0.12	0.2 - 3.1
EAST	3.1 - 24.6	0.39 - 7.53	2.4 - 9.6	0.04 - 0.15	0.2 - 3.3
WEST	2.4 - 24.8	0.21 - 5.42	1.9 - 9.7	0.03 - 0.15	0.2 - 3.5
NORTH (not used)	*6.3 - 74.4*	*0.48 - 24.83*	*5.0 - 29.2*	*0.08 - 0.46*	*0.5 - 7.4*

Table 6. Eruption velocity, maximum amplitude, and instantaneous and cumulative flux are calculated from 36 selected events at all four stations that represent a wide range of amplitudes and frequencies seen in discrete signals at West Mata. The South station's values were calculated assuming spherical spreading; all other stations use cylindrical spreading of sound. Because multipathing compromises results from the north station, numbers from that station are not used when determining the range of eruption velocities, flux, and volume at West Mata, although their numbers are reported here.

Table 7a

METHOD	NUMBER OF EVENTS PICKED	MAX AMPLITUDE (range, Pa)	u (range, m/s)	CUMULATIVE ERUPTIVE VOLUME (m^3)
Hand-picked	5272	0.13 - 19.92	1.0 - 31.8	21 - 337
Auto-picked	10966	0.05 - 19.48	0.8 - 33.2	41.5 - 667.2

Table 7b (hand-picked)

YEAR - JULIAN DAY, TIME FRAME	NO. OF EVENTS PICKED	MAX AMP (range, Pa)	u (range, m/s)	CUMULATIVE VOLUME (m^3)
2009 - 348, 10:10 - 10:40	374	0.22 - 10.20	1.5 - 23.8	1.1 - 17.5
2009 - 356, 01:30 - 02:00	470	0.19 - 7.38	1.5 - 18.2	1.9 - 29.7
2009 - 363, 04:19 - 04:49	424	0.35 - 5.65	1.6 - 17.2	1.7 - 26.6
2010 - 004, 16:05 - 16:33	206	0.24 - 14.01	1.4 - 27.2	0.8 - 13.2
2010 - 018, 17:38 - 18:07	405	0.09 - 3.04	1.0 - 14.4	1.1 - 17.6
2010 - 043, 01:35 - 02:04	408	0.34 - 11.78	2.1 - 31.8	1.6 - 26.1
2010 - 049, 15:49 - 16:18	748	0.21 - 6.86	1.6 - 18.0	2.8 - 45.1
2010 - 062, 20:29 - 20:58	329	0.55 - 7.60	2.4 - 21.4	1.7 - 27.8
2010 - 073, 15:05 - 15:34	539	0.31 - 8.54	2.0 - 17.8	2.4 - 39.0
2010 - 093, 02:59 - 03:28	568	0.47 - 19.92	1.5 - 30.8	2.7 - 43.2
2010 - 101, 04:00 - 04:29	801	0.24 - 8.29	1.2 - 18.4	3.2 - 51.4

Table 7c (auto-picked)

YEAR - JULIAN DAY, TIME FRAME	NO. OF EVENTS PICKED	MAX AMP RANGE (Pa)	u (range, m/s)	CUMULATIVE VOLUME (m^3)
2009 - 348, 10:10 - 10:40	743	0.08 - 11.45	0.9 - 24.2	2.0 - 31.4
2009 - 356, 01:30 - 02:00	897	0.12 - 6.06	1.2 - 16.2	3.0 - 48.8
2009 - 363, 04:19 - 04:49	576	0.15 - 7.03	1.3 - 20.6	2.2 - 35.4
2010 - 004, 16:05 - 16:33	720	0.08 - 14.01	1.0 - 25.4	2.2 - 35.7
2010 - 018, 17:38 - 18:07	1102	0.11 - 4.07	1.0 - 16.2	3.3 - 52.5
2010 - 043, 01:35 - 02:04	887	0.18 - 11.78	1.3 - 26.0	3.6 - 58.4
2010 - 049, 15:49 - 16:18	1135	0.08 - 6.86	1.0 - 18.6	4.6 - 74.0
2010 - 062, 20:29 - 20:58	976	0.23 - 19.48	1.5 - 33.2	4.8 - 77.3
2010 - 073, 15:05 - 15:34	1314	0.11 - 7.33	1.1 - 19.6	5.2 - 82.7
2010 - 093, 02:59 - 03:28	1232	0.10 - 9.13	1.2 - 22.2	5.4 - 87.2
2010 - 101, 04:00 - 04:29	1384	0.05 - 7.35	0.8 - 20.2	5.2 - 83.8

Table 7. Total differences in number of events picked, maximum amplitude, range of eruption velocity, and cumulative flux for hand-picked events compared to automatically-picked for a 5.5 hour time frame (a). Numbers for each day for hand-picked (b) and automatically-picked (c) are also listed. These values are calculated from only the south station.

BUBBLE NUMBER	INSTANTANEOUS VELOCITY (m/s)	
	bubble diameter = 1.0 m	bubble diameter = 0.25 m
1	3.3	0.4
2	4.0	0.5
3	1.7	0.2
4	2.2	0.3
5	3.2	0.4
6	3.1	0.4
7	2.2	0.3
8	2.7	0.3
9	2.4	0.3
10	3.3	0.4
11	3.0	0.4
12	1.4	0.2
13	2.8	0.3
14	1.7	0.2
15	2.3	0.3
16	3.2	0.4
17	3.3	0.4
18	5.3	0.7
RANGE	**1.4 - 5.3 m/s**	**0.2 - 0.7 m/s**
RANGE: 0.2 - 5.3 m/s		

Table 8. Range of instantaneous eruption velocities of 18 gas bubble explosions using the video adapted from Joseph Resing (NOAA/PMEL).

METHOD	ERUPTIVE VELOCITY (m/s)	ERUPTIVE FLUX PER EVENT (m^3/s)	CUMULATIVE VOLUME (m^3/yr)
STA/LTA with hydroacoustic data *(instantaneous)*	1.0 - 31	0.1 - 24	total volume (lava + gas): **$5.7 \times 10^3 – 9.1 \times 10^4$**
			lava only (25% vesicularity), d.t. = 1.8: **$9.6 \times 10^2 – 2.8 \times 10^4$**
			lava only (25% vesicularity), d.t. = 1.5: **$1.9 \times 10^4 – 5.6 \times 10^6$**
Ken Rubin's frame-by-frame video *(instantaneous)*	0.4 - 1.5	0.02 - 1.2	**$1.2 \times 10^6 – 1.1 \times 10^8$**
Joe Resing's frame-by-frame video *(instantaneous)*	0.2 - 5.3	0.4 - 4.2	**$3.0 \times 10^4 – 5.6 \times 10^6$**
Clague's bathymetric estimate *(long-term)*	N/A	N/A	**5.7×10^6**

Table 9. Results from this study (using acoustic pressure to calculate eruption velocity), as well as alternative methods for calculating eruption velocity and yearly flux at West Mata. Volumes are given for lava only. (d.t. = "detection threshold.")

VI. The technique: Can hydroacoustic data be used for studying submarine eruptive flux at other volcanoes?

In this study, the range of instantaneous eruption velocities was calculated from discrete gas bubble explosions at West Mata volcano in the Lau Basin. These velocities were used to calculate instantaneous flux and a range of values for yearly eruption volume associated with explosive bursts at West Mata during the 5-month hydrophone deployment. I now address whether or not this method is reliable enough to be used at other submarine volcanoes in calculating eruption velocity and cumulative volume.

Signal reflections – which alter the shape and amplitude of the signals – create two problems when using this method. First, because the reflected signals arrive before the end of the signal recorded by the direct wave, only the first 20 ms of the waveform can be used on each station, instead of the entire waveform. The signal reflections also make it impossible to use acoustic pressure to calculate eruption velocity and cumulative volume for prolonged signals, such as the diffuse events associated with effusive eruptions. The method used by Vergniolle and Caplan-Auerbach (2006) and Caplan-Auerbach et al. (2010) to calculate eruption velocity for continuous signals could be used to calculate eruption velocity from diffuse signals recorded by hydrophones in the near field, where sea surface reflections would not be an issue, and signal contamination would not occur.

Because multipathing amplified signals at the north station, results from the north station were ignored in comparing results from this study to previous studies and alternative methods for measuring eruption velocity. Ranges of eruption velocities from the south, east, and west stations calculated in this study (1.0 – 31 m/s) are consistent with, albeit slightly higher, than values calculated from the alternative methods (0.2 – 5.3 m/s). Many of the

velocities calculated from discrete events are on the same order of magnitude using all methods, and enough overlap of these values is observed to conclude that acoustic pressure can be used to calculate eruption velocity in the submarine environment. It is important that eruption velocity is not significantly affected by the size of the gas bubbles at the vent, and thus eruption velocities in this study can be considered to be reliable

Yearly volume rates from this study are two to three orders of magnitude smaller than those given in other studies (Chadwick et al., 2008b; Walker et al., 2008; Clague et al., 2011).

Because only a portion of signals (discrete, which account for less than 50% of signal types) were able to be used for calculations in this study, the cumulative volumes should be expected to be smaller than those from other studies. Furthermore, because volume calculations are dependent on the number of discrete events used for calculations, as well as the gas bubble size, accuracy of yearly eruptive volume is limited. Greater emphasis should be placed on using hydroacoustic pressure to accurately calculate eruption velocities in the submarine environment.

There are complications that exist in the submarine environment (e.g., sea surface reflections introduced by signal multipathing) that are otherwise not a problem in the subaerial, and future studies would have to address these issues in order to capture a more accurate picture of the eruptive behavior and calculating eruptive volume seen at West Mata volcano by using hydroacoustic signals.

VII. CONCLUSIONS

The original goals of this study were to calculate a range of eruption velocities and estimate cumulative eruptive volume at West Mata volcano in the Lau Basin during a 5-month hydrophone deployment. After detecting events representing gas bubble explosions, we were able to use equations from Lighthill (2001) relating acoustic power to velocity to calculate eruption velocity and volume. Results from this study yield eruption velocities up to one order of magnitude larger than other studies, and cumulative volumes that are two to three orders of magnitude smaller than those reported in other studies. Gas bubbles from the video imagery at West Mata used to estimate eruption velocities likely represented the larger end-member of sizes, and should be expected to have lower eruption velocities than gas bubbles that are smaller, or a number of gas bubbles that represent a range of sizes (which is assumed to be the case for this study). Because only a portion of the signals from this study could be used to estimate cumulative eruptive volume, results are expected to be lower than those from other studies, suggesting that this technique is viable for a network of near-field hydrophones in the submarine environment. The range of eruptive velocities seen at the south station for the portion of hand-picked explosions was 1.0 – 31.0 m/s. Based on these hand-selected explosions at the south station, the total eruptive volume at West Mata translates to a rate of $5.7 \times 10^3 – 9.1 \times 10^4$ m^3/yr for both lava and gas, or $1.9 \times 10^3 – 5.6 \times 10^4$ m^3/yr for lava only (assuming 25% vesicularity, and using a detection threshold of 1.5; Merle, 2012).

There are several limitations to this method. The first limitation is a byproduct of signal reflections, which necessitate that only the first 20 ms of discrete signals can be used for calculations, and requires that diffuse signals be excluded from calculations. The second

limitation is that the automatic detection of events did not adequately separate gas bubble explosions from other signals. This inhibits total automation of this method, and requires events to be picked by hand and extrapolated for total eruptive volume.

West Mata's distribution of amplitudes varied as frequently as an hourly basis, which made it impossible to apply a b-value that would allow accurate extrapolation for cumulative flux, as well as decrease the amount of time spent processing data.

After completing this study, the final conclusion is that this method for calculating eruption velocity and cumulative volume using hydroacoustic pressure yields reasonable results for hydrophones located in the near-field (<5 km). However, signal multipathing (including complications with reflected signals and altered amplitudes) introduces uncertainty, reflecting the complex nature of the submarine environment. Total volumetric estimates cannot be accurately calculated, because only a portion of the signals (discrete signals only) could be used to calculate eruption velocity. Further studies are needed to find a method that can use hydroacoustic signals from a variety of eruptive styles to calculate eruptive velocities, which would also provide a more accurate estimate of the total eruptive volume. It is also necessary for future studies to consider the distances and depths at which hydrophone stations are deployed, in order to eliminate complications from signal multipathing. Groundtruthing these calculations with a greater abundance of video observation using remotely operated vehicles (ROVs) would solidify confidence in the calculated eruption velocity and cumulative volume.

VIII. LIST OF REFERENCES

Barbour, L.H. and Woollard, G.P., 1949. Sofar triangulation methods, Woods Hole Oceanographic Institute.

Baumberger, T., Lilley, M.D., Lupton, J.E., Resing, J.A., Baker, E.T., Walker, S.L., Rubin, K.H, and Frueh-Green, G.L., 2009. Hydrogen and Methane Dissolved in Plumes of the Northeast Lau Basin Eruption Sites. American Geophysical Union: Abstracts with Programs, #V431-04.

Bohnenstiel, D.R., Dziak, R.P., Matsumoto, H., Lau, T.A., Fowler, M., Schiep, C., Cook, K.E., Warren, K.W., Conder, J.A., and Wiens, D.A., 2010. Hydroacoustic Monitoring of Seismic and Volcanic Activity within the Lau Basin (Invited). American Geophysical Union: Abstracts with Programs, #T11E-02.

Caplan-Auerbach, J., and Duennebier, F., 2001. Seismicity and velocity structure of Loihi seamount from the 1996 earthquake swarm: Bulletin of the Seismological Society of America, vol. 91, no. 2, pp. 178-190.

Caplan-Auerbach, J., Bellesiles, A., and Fernandes, J.K., 2010. Estimates of eruption velocity and plume height from infrasonic recordings of the 2006 eruption of Augustine Volcano, Alaska: Journal of Volcanology and Geothermal Research, vol. 189, issues 1-2, p. 12-18.

Chadwick, W.W. Jr., Wright, I.C., Schwarz-Schampera, U., Hyvernaud, O., Reymond, D., and de Ronde, C.E.J., 2008a. Cyclic eruptions and sector collapses at Monowai submarine volcano, Kermade arc: 1998-2007: Geochemistry, Geophysics, Geosystems, vol. 9, no. 10.

Chadwick, W.W. Jr., Cashman, K.V., Embley, R.W., Matsumoto, H., Dziak., R.P., de Ronde, C.E.J., Lau, T.K., Deardorff, N.D., and Merle, S.G., 2008b. Direct video and hydrophone observations of submarine explosive eruptions at NW Rota-1 volcano, Mariana arc: Journal of Geophysical Research, vol. 113, 23 pp.

Clague, D.A., Paduan, J.B., Caress, D.W., Thomas, H., Chadwick, W.W. Jr., and Merle, S.G., 2011. Volcanic morphology of West Mata Volcano, NE Lau Basin, based on high-resolution bathymetry and depth changes: Geochemistry, Geophysics, Geosystems, vol. 12., no. 11.

Deardorff, N. D., Cashmn, K. V., Chadwick, W. W. Jr., 2011. Observation of eruptive plume dynamics and pyroclastic deposits from submarine explosive eruptions at NW Rota-1, Mariana arc: Journal of Volcanology and Geothermal Research, vol. 202, p. 47-59.

DOSITS website: Discovery of Sound In The Sea. www.dosits.org.

Dziak, R.P., Bohnenstiehl, D.R., Matsumoto, H., Fowler, M.J., Haxel, J.H., Tolstoy, M., and Waldhauser, F., 2009. January 2006 seafloor-spreading event at 9°50'N, East Pacific Rise: Ridge dike intrusion and transform fault interactions from regional hydroacoustic data: Geochemistry, Geophysics, Geosystems, vol. 10, no. 6, 14 pp.

Dziak, R., Bohnenstiehl, D.R., Baker, E.T., Matsumoto, H., Haxel, J., Walker, S., and Fowler, M., 2010. Volcanic Explosions, Seismicity, and Debris from the West and North Mata Volcano Complex, NE Lau Basin. American Geophysical Union: Abstracts with Programs, #T13B-2186.

Dziak, R.P., Baker, E.T., Shaw, A.M., Bohnenstiehl, D.R., Chadwick, Jr., W.W., Haxel, J.H., Matsumoto, H., and Walker, S.L., 2012. Flux measurements of explosive degassing using a yearlong hydroacoustic record at an erupting submarine volcano: Geochemistry, Geophysics, Geosystems, vol. 13, no. 11, 13:Q0AF07. doi:10.1029/2012GC004211.

Embley, R.W., Chadwick, W.W. Jr., Clague, D., and Stakes, D., 1999. 1998 eruption of Axial volcano: multibeam anomalies and seafloor observations: Geophysical Research Letters, vol. 26, issue 23, pp. 3425 – 3428.

Embley, R.W. et al., 2006. Long-term eruptive activity at a submarine arc volcano: Nature, vol. 441, pp. 494-497.

Fee, D., Garces, M., Patrick, M., Chouet, B., Dawson, P., and Swanson, D., 2010. Infrasonic harmonic tremor and degassing bursts from Halema'uma'u Crater, Kilauea Volcano, Hawaii: Journal of Geophysical Research, vol. 115, B11316.

Fee, D. and Matoza, R.S., 2013. An overview of volcano infrasound: From hawaiian to plinian, local to global: Journal of Volcanology and Geothermal Research, vol. 249, pp. 123 – 139.

Green, D.N., Evers, L.G., Fee, D., Matoza, R.S., Snellen, M., Smets, P., and Simons, D., 2013. Hydroacoustic, infrasonic and seismic monitoring of the submarine eruptive acticity and sub-aerial plume generation at South Sarigan, May 2010: Journal of Volcanology and Geothermal Research, vol. 257, pp. 31-43.

Hagerty, M.T., Schwartz, S.Y., Garces, M.A., and Protti, M., 2000. Analysis of seismic and acoustic observations at Arenal Volcano, Costa Rica, 1995-1997: Journal of Volcanology and Geothermal Research, vol. 101, pp. 27-65.

Jensen, Finn B., et al., 1993. Computational Ocean Acoustics: AIP Press, pp. 10 – 15.

Johnson, J.B. and Lees, J.M., 2000. Plugs and chugs – seismic and acoustic observations of degassing explosions at Karymsky, Russia and Sangay, Ecuador: Journal of Volcanology and Geothermal Research, 67-82.

Johnson, J.B., 2003. Generation and propagation of infrasonic airwaves from volcanic explosions: Journal of Volcanology and Geothermal Research, vol. 121, pp. 1 – 14.

Lees, J.M., Gordeev, E.I., and Ripepe, M., 2004. Explosions and periodic tremor at Karymsky volcano, Kamchatka, Russia, Geophysical Journal International, vol. 158, pp. 1151-1167.

Lees, J. M., Johnson, J. B., Ruiz, M., Troncoso, L., and Welsh, M., 2008. Reventador Volcano 2005: Eruptive activity inferred from seismo-acoustic observation: Journal of Volcanology and Geothermal Research, vol. 176, p. 179-190.

Lighthill, J., 2001. Waves in Fluids, 2nd ed. Cambridge University Press, Cambridge, U.K. 520 pp.

Matoza, R. S., Hedlin, M. A.H., Garcés, M. A., 2007. An infrasound array study of Mount St. Helens: Journal of Volcanology and Geothermal Research, v. 160, pp. 249-262.

Matoza, R.S., Fee, D., and Garces, M.A., 2010. Infrasonic tremor wavefield of the Pu'u 'O'o crater complex and lava tube system, Hawaii, in April 2007: Journal of Geophysical Research, vol. 115, B12312.

Merle, S., 2008, Northeast Lau Basin, Cruise Report on R/V Thompson Expedition TN227, November 13-28, 2008, Apia to Apia, Western Samoa.

Merle, S., 2009, Northeast Lau Basin Response Cruise (NELRC), Cruise Report on R/V Thomas G. Thompson Expedition TN-234, May 5-13, 2009, Apia Samoa – Apia Samoa, Jason-2 Dives J2-413 to J2-420.

Merle, S., 2012, Submarine Ring of Fire-2012 (SroF-12) Northeast Lau Basin, Cruise Report on R/V Roger Revelle Expedition RR1211, Sept 9 – 25, 2012, Suva Fiji to Apia Samoa, Quest 4000 Dives Q322 to Q333.

Moore, J.G., Clague, D.A., and Normark, W.R., 1982. Diverse basalt types from Loihi seamount, Hawaii: Geological Society of America, vol. 10, no. 2, pp. 88-92.

Munk, Walter, 2006. Physical Oceanography: Developments since 1950: Springer, pp. 119-138.

Petersen, T., De Angelis, S., Tytgat, G., and McNutt, S. R., 2006, Local infrasound observations of large ash explosions at Augustine Volcano, Alaska, during January 11-28, 2006: Geophysical Research Letters, vol. 33, L12303.

Resing, J., Embley, R., and Rubin, K., 2009, Eruptions in the NE Lau Basin: MARGINS Newsletter No. 23, Fall 2009 (12-15).

Resing, J., and others, 2011, Active submarine eruption of boninite in the northeastern Lau Basin: Nature Geoscience, vol. 4, pp. 799-806.

Ripepe, M., Poggi, P., Braun, T., and Gordeev, E., 1996. Infrasonic waves and volcanic tremor at Stromboli: Geophysical Research Letters, vol. 23, no. 2, pp. 181-184.

Rowe, C.A., Aster, R.C., Kyle, P.R., Dibble, R.R., and Schlue, J.W., 2000. Seismic and acoustic observations at Mount Erebus Volcano, Ross Island, Antarctica, 1994-1998: Journal of Volcanology and Geothermal Research, vol. 101, pp. 105-128.

Speaks, Charles E., 1992, Introduction to Sound: Acoustics for the Hearing and Speech Sciences: Singular Publishing Group Inc., 308 p.

Tolstoy, I. and Clay, C., 1987, Ocean Acoustics: Theory and Experiment in Underwater Sound: Acoustical Society of America, 293 p.

Urick, Robert J., 1975, Principles of Underwater Sounds: McGraw Hill, 384 p.

Vergniolle, S., and Brandeis, G., 1994, Origin of the sound generated by Strombolian explosions: Geophysical Research Letters, vol. 21, no. 18, pp. 1959-1962.

Vergniolle, S. and Brandeis, G., 1996, Strombolian explosions, 1. A large bubble breaking at the surface of a lava column as a source of sound: Journal of Geophysical Research, vol. 101, no. B9, pp. 20,433-20,447.

Vergniolle, S., Brandeis, G., and Mareschal, J.-C., 1996, Strombolian eruptions: 2. Eruption dynamics determined from acoustic measurements: Journal of Geophysical Research, vol. 101, no. B9, pp. 20,449-20,466.

Vergniolle, S., Boichu, M., and Caplan-Auerbach, J., 2004: Acoustic measurements of the 1999 basaltic eruption of Shishaldin volcano, Alaska, 1. Origin of Strombolian Activity: Journal of Volcanology and Geothermal Research, vol. 137, pp. 109-134.

Vergniolle, S., and Caplan-Auerbach, J., 2004: Acoustic measurements of the 1999 basaltic eruption of Shishaldin volcano, Alaska, 2. Precursor to the Subplinian phase: Journal of Volcanology and Geothermal Research, vol. 137, pp. 135-151.

Vergniolle, S., and Caplan-Auerbach, J., 2006. Basaltic thermals and Subplinian plumes: Constraints from acoustic measurements at Shishaldin volcano, Alaska: Bulletin of Volcanology, vol. 68, pp. 611-630.

Walker, S.L., Baker, E.T., Resing, J.A., Chadwick, Jr., W.W., Lebon, G.T., Lupton, J.E., and Merle, S.G., 2008. Eruption-fed particle plumes and volcaniclastic deposits at a submarine volcano: NW Rota-1, Mariana Arc: Journal of Geophysical Research, vol. 113, B08S11, doi:10.1029/2007JB005441.

White, J.D., Smellie, J.L., and Clague, D.A., 2003a. Introduction: a deductive outline and topical overview of subaqueous explosive volcanism: Explosive subaqueous volcanism, no. 140, Geophysical Monograph Series, AGU, pp. 1-23.

Woulff, G., and McGetchin, T.R., 1976. Acoustic Noise from Volcanoes: Theory and Experiment: Geophysical Journal of Research, vol. 45, pp. 601-616.

Zellmer, K.E., and Taylor, B., 2001. A three-plate kinematic model for Lau Basin opening: Geochemistry, Geophysics, Geosystems, vol. 2, paper number 2000GC000106.

IX. APPENDICES

All appendix material is listed and described here. Videos, scripts, and other files can be found on the supplemental CD inside the back cover of this thesis.

APPENDIX I – VIDEOS

• Quench_Cap – *video showing the quench cap of lava seen at Hades vent.*

• 45_seconds_degassing – *video recording of 45 seconds of continuous degassing at Hades vent.*

• 18_bubbles_WM – *edited version of the video "45_seconds_degassing" showing a series of 18 gas bubble bursts at Hades vent. Each bubble burst is slowed down to 1/8 of the original speed.*

APPENDIX II – SCRIPTS

• cm_mata_spec.m – *Script used to generate spectrograms for a given series of time from the data on all four stations. The figure generated will contain both the waveforms and its corresponding spectrogram. If a spectrogram for only one station is desired, the scripts "cm_mata_spec_S.m," "cm_mata_spec_E.m," "cm_mata_spec_W.m," and "cm_mata_spec_N.m" may be used. Adapted from the original script "mata_spec.m" written by Jackie Caplan-Auerbach.*

• hydrophone_corr.m – *Converts raw hydrophone data from count to Pascals. Courtesy of Del Bohnenstiehl.*

• lta_sta_velflux_S.m – *A multi-step script that first identifies events for a given amount of time from the data, and then calculates the eruption velocity and flux for each event. This script will generate a table that records the eruption velocity, flux, acoustic power, event duration, maximum amplitude, and detection threshold for each event identified. This version must be executed by hand-selecting events that are identified; if complete automation of these steps is desired, then the script "lta_sta_velflux_autoS.m" may be used. Additionally, the scripts "lta_sta_velflux_E.m," "lta_sta_velflux_W.m," and "lta_sta_velflux_N.m" can be used for calculations at the other stations.*

• bvalue.m – *Calculates the b-value for a given time period from the data.*

APPENDIX III – OTHER

• Frame_by_frame – *Powerpoint that shows a frame-by-frame shot of a bubble explosion at West Mata. Each frame is 0.13 seconds long. Courtesy of Joseph Resing.*

• master_list_36events – *Excel file containing the time frames and detection thresholds at which the 36 hand-selected events from table 6 can be found.*